Low-Cost Manufacturing of Electrokinetic Preconcentration Systems

By

Eric Wynne
B.S., Engineering Physics
University of Illinois at Urbana-Champaign, 2022

Submitted to Department of Electrical Engineering and Computer Science in Partial Fulfillment of the Requirements for the Degree of

Master of Science in Electrical Engineering and Computer Science
at the
Massachusetts Institute of Technology
May 2022

Signature of Author.....

Department of Electrical Engineering and Computer Science
April 29, 2022

Certified by.....
Jongyoon Han
Professor of Electrical Engineering and Biological Engineering
Thesis Supervisor

Accepted by.....
Leslie A. Kolodziejski
Professor of Electrical Engineering and Computer Science
Chair, Department Committee on Graduate Students

Low-Cost Manufacturing of Electrokinetic Preconcentration Systems

By
Eric Michael Wynne

Submitted to the Department of Electrical Engineering and Computer Science on April 26th, 2022 in Partial Fulfilment of the Requirements for the Degree of Master of Science at the Massachusetts Institute of Technology

ABSTRACT

Detection of low-abundance biomolecules is a critical challenge in improving the safety and efficacy of pharmaceuticals. The methods and technologies for detecting DNA, RNA, and proteins have increased in sensitivity such that even single copies can be detected in certain conditions. However, due to diffusion limited transport of the biomolecules to sensors, these emerging biosensing technologies are only able to process a very small fraction of sample volume available. Therefore, there is a need for technology that can reduce the sampling error by concentrating the relevant molecules into a volume compatible with the sensing technology.

Here we present a low-cost, manufacturable implementation of a sample preconcentration device that uses the ion concentration polarization phenomena to filter charged biomolecules from a solution. Compared to previous electrokinetic concentrators, our device prioritizes manufacturability and sample throughput so that there is a simple path to deploying the device in the biological labs and even field-based detection in the future. We demonstrate the stabilizing effect of microscale fluidic features in electrokinetic concentrators by characterizing device performance with various feature dimensions. We also characterize the preconcentration performance as a function of the applied voltage and the pressure-driven flow velocity. Finally, we explore alternate device designs made possible by our low-cost manufacturing methods and materials, to provide a guide for future improvements. Ultimately, our work demonstrates a novel fabrication method that could be generalized to other devices and bring electrokinetic concentrators closer to broader adoption outside of the microfluidics research community.

Thesis Supervisor: Jongyoon Han
Title: Professor of Electrical Engineering and Biological Engineering

Acknowledgements

Special thanks to Professor Jongyoon Han for his mentorship and support. I greatly appreciate his vision and patience that allowed me to find a project I am passionate about in a field that was new to me. He has consistently motivated me to be curious and optimistic in my work.

Thanks to current and past members of the Han Lab who helped me learn and inspired me with their accomplishments. I am lucky to have such a kind and talented group of colleagues.

I would also like to thank David Lewis and Anthony Pennes from the Cypress Engineering Design Studio for helping me move my fabrication out of the cleanroom and into the workshop.

Thanks to my friends and family for their love and support, everything is possible because of them.

Lastly, thanks to the Singapore-MIT Alliance for Research and Technology (SMART) CAMP project for making this work possible

Table of Contents

List of Figures

List of Tables

Chapter 1 Introduction

1.1 The Importance of Low Abundance Molecular Detection

Analysis of relatively low abundance biomolecules—such as proteins and DNA—is becoming increasingly important in clinical and bio-manufacturing contexts. For example, Chimeric Antigen Receptor T cell (CAR-T) therapy products must undergo a variety of tests to screen for bacterial and fungal contaminants, replication-competent viruses, and other impurities leftover from the manufacturing process[1–5]. These organisms and other molecular impurities, which threaten the efficacy and safety of pharmaceutical products, are called adventitious agents. Adventitious agents pose a uniquely grave safety risk in cell therapy products because patients receiving the therapy are already at risk for other complications such as cytokine release syndrome and neurotoxicity caused by the CAR-T cells[6–8]. Extremely low concentrations (as low as 1-10 CFU or PFU per ml) of adventitious agents could go undetected by testing at one point in production, allowing them to multiply during the storage or transport of the product.

Biomanufacturing of vaccines is also at risk from adventitious agents, and viral contamination has temporarily affected vaccine availability and posed possible risks to public health[9–11]. Therefore, to ensure the sterility of vaccines, it would be ideal to test the final products and raw materials with highly sensitive yet non-targeted methods, such as high-throughput sequencing[12,13].

The sensing technology needed for low abundance detection has made significant progress, and in certain circumstances it is now possible to detect even single copies of protein or genetic material. There has been significant interest in using next generation sequencing for adventitious agent detection because it is a non-targeted yet sensitive approach that could be used to find viruses and bacteria[13–17]. Targeted DNA detection methods such as polymerase chain reaction (PCR) have proven useful in low abundance pathogen detection by using the process of DNA amplification[18–20]. Newer methods like droplet digital PCR (ddPCR) and quantitative PCR (qPCR) are both highly sensitive and able to quantify the number of initial target DNA copies[21,22].

Low abundance protein detection may also prove useful for clinical diagnostics and biologics quality assurance (*e.g.*, endotoxin detection). For example, single molecules of cancer marker proteins have been detected using label-free photonic resonators that produce frequency shifts in the presence of a protein molecule[23]. Additionally, carbon nanotubes have been used to detect single copies of HIV integrase using label-free fluorescence based recognition[24]. In the case of non-nucleotide biomolecules, the lack of amplification strategy makes it even more challenging to detect low-abundance targets.

To summarize, there already exists a variety of technologies with sufficiently high sensitivity to be used for sterility testing, but the utility of these tests could be improved by adding a preconcentration process.

1.2 The Fundamental Need for Preconcentration

The reason why highly sensitive biosensors operate using only small sample volumes was thoroughly described by Squires *et al.*[25] using simulations and molecular transport theory. The Peclet number (Pe) is a dimensionless quantity that describes the ratio between diffusion and advection in a system. **Equation 1-1** describes the Peclet number in which L is the characteristic length, D is the diffusion coefficient, and U is the flow velocity.

$$\mathrm{Pe} = \frac{\text{Diffusion Time}}{\text{Advection Time}} = \frac{L}{D*U} \tag{1-1}$$

In the case of a biosensor in which the transducer is a surface, such as the flow cell in a nanopore sequencing device, it is intuitive to think of the Peclet number as the time it takes a molecule to diffuse from the complete opposite side of a channel to the transducer divided by the time it takes the molecule to flow past the transducer. A low Peclet number (Pe<<1) would mean nearly all molecules have sufficient time for diffusing to the transducer and being detected before flushed away, while a high Peclet number (Pe>>1) means that most molecules are flowing past the transducer and being missed.

Sensors with high sensitivity need to minimize the Peclet number to ensure that low abundance molecules are not missed. To minimize the Peclet number only two aspects of a sensor can be changed—the device dimensions and sample flowrate—because the diffusion coefficient is inherent to each molecule being detected. Small shallow channels and low flowrates are needed to sufficiently decrease the Peclet number, and this simultaneously decreases the volume of sample that can be processed by a device. Therefore, for applications

in which high sensitivity is required—such as sterility testing—there will be a mismatch between large sample volumes and small analyzed volumes, and the sampling error can be greatly reduced by concentrating the relevant molecules into a smaller volume. Examples illustrating the mismatch between the volume of relatively small scale culture methods associated with pharmaceutical research and the volume of adventitious agent detection methods can be seen in **Table 1-1**.

Table 1-1

Sample Volume	Analysis Volume
T Flask – Several milliliters	Magnetic Bead Assay - 100µl
Spinner Flask – Hundred milliliters	Digital Droplet PCR – 20µl
Culture Bag – 1 Liter	Nanopore Sequencing - 75µl

1.3 Proven Utility of Electrokinetic Concentrators

Proof-of-concept Electrokinetic (EK) concentrators have already proven useful in several areas of application. A popular application of EK concentration technology has been to increase the limit of detection for assays. The speed of a DNA surface hybridization assay has been increased by two orders of magnitude, allowing 1 nM concentrations of the targeted DNA to be detected within 15 minutes[26]. A multistage device was able to concentrate HIV p24 protein such that concentration as low as 10 aM became detectable using fluorescent

labeling, a detection limit 5 orders of magnitude lower than a comparable ELISA assay[27]. EK concentration can also enhance ELISA, in one case increasing the sensitivity of a prostate specific antigen assay 100 fold by trapping beads near the concentrated molecules[28].

Additionally, the scope of EK concentrators has been increasing due to research into modifying samples to be more compatible with EK concentration. Typically EK concentration has been limited to enrichment of charged molecules, but it has been shown that adding a surfactant such as sodium dodecyl sulfate can make it possible to focus even neutral species with high efficiency[29]. Surfactant molecules can accumulate on neutral species and turn it into a micelle with net charge. Extraction efficiency of weakly charged and uncharged molecules can also be improved using a process called molecular charge modulation (MCM). With MCM custom peptides can be designed to add positive or negative charge to targeted molecules, thereby changing the electrophoretic mobility of the target[30].

EK concentrators have also been used continuously as filters usually by having separate outlets for a concentrated stream and the filtrate[31]. In human blood plasma albumin was able to be separated from neutral metabolites with the goal of using the filtrate as dialysate in a miniaturized hemodialysis device[32]. High-throughput EK filters have been able to separate oil emulsions from water at rates of up to 40,000 $L/H^{*}m^{2}$, potentially having implications for more efficient wastewater treatment[33].

In summary, EK concentrator technology has matured rapidly over the past two decades and it is well positioned to make a significant impact once deployed for use in the real world.

1.4 Challenges of Electrokinetic Concentration

Though proof-of-concept EK concentrators have produced exciting results in several areas of applications there are important challenges with the technology that must be solved on the way to deploying devices for use in the real world. While much of the prototyping of EK concentrators has taken place using conventional PDMS microfluidic channels, most commercialized microfluidic devices do not use PDMS due to issues with cost and large scale manufacturing[34]. In comparison to thermoplastic injection molding, large scale PDMS manufacturing is complicated and still an area of active research[35,36]. Additionally, transitioning prototype devices from PDMS to materials like thermoplastics is not trivial because differences in properties such as deformability can drastically affect device performance[37]. Therefore, it would be advantageous to begin prototyping EK concentrators with manufacturing scalability in mind when choosing materials and processes.

Sample throughput is also an area that generally needs improving for EK concentrators. Pressure driven flow is often generated in EK concentrators by filling reservoirs with different volumes, leading to low flowrates on the scale of nanoliters[32,38–40]. Higher flowrates would increase the utility of concentrators by making them compatible volumes typically associated with biomanufacturing. However, increasing device scale and flowrate has been held back by the need to control electroosmotic instability, a phenomena that can cause device failure and is an active area of research[41–43]. Small channel dimensions and lithographically patterned microstructures have been used in previous microfluidic devices[44],

but additional strategies for stabilization will need to be created as we scale up to *milifluidic* devices and beyond.

1.5 Thesis Scope

The goal of this work is to demonstrate a device that translates existing electrokinetic concentrators to a more manufacturable and reproducible design. First, we introduce and explain the physics associated with the ion concentration polarization phenomenon to provide a basis for understanding how EK concentrators function (Chapter 2). We then discuss the merits and drawbacks of previous EK concentrators designs and describe our novel design and manufacturing process (Chapter 3). We propose and confirm the functionality of our new design and validate our assumption about relationship between minimum channel features size and device stability that makes our large-channel device feasible. We also explore the effect of operational parameters such as applied bias and pressure upon concentration performance. Finally, we briefly explore alternate device designs made possible by using the same general, low-cost materials and processes involved in manufacturing our device.

1.6 References

1. Levine, B. L., Miskin, J., Wonnacott, K. & Keir, C. Global Manufacturing of CAR T Cell Therapy. *Mol. Ther. - Methods Clin. Dev.* **4**, 92–101 (2017).

2. Reddy, O. L., Stroncek, D. F. & Panch, S. R. Improving CAR T cell therapy by optimizing critical quality attributes. *Semin. Hematol.* **57**, 33–38 (2020).

3. Li, Y., Huo, Y., Yu, L. & Wang, J. Quality Control and Nonclinical Research on CAR-T Cell Products: General Principles and Key Issues. *Engineering* **5**, 122–131 (2019).

4. Tyagarajan, S., Spencer, T. & Smith, J. Optimizing CAR-T Cell Manufacturing Processes during Pivotal Clinical Trials. *Mol. Ther. - Methods Clin. Dev.* **16**, 136–144 (2020).

5. Eyles, J. E. *et al.* Cell therapy products: focus on issues with manufacturing and quality control of chimeric antigen receptor T-cell therapies. *J. Chem. Technol. Biotechnol.* **94**, 1008–1016 (2019).

6. Brudno, J. N. & Kochenderfer, J. N. Toxicities of chimeric antigen receptor T cells: recognition and management. *Blood* **127**, 3321–3330 (2016).

7. Lee, D. W. *et al.* Current concepts in the diagnosis and management of cytokine release syndrome. *Blood* **124**, 188–195 (2014).

8. Turtle, C. J. *et al.* CD19 CAR-T cells of defined CD4+:CD8+ composition in adult B cell ALL patients. *J. Clin. Invest.* **126**, 2123–2138 (2016).

9. Petricciani, J., Sheets, R., Griffiths, E. & Knezevic, I. Adventitious agents in viral vaccines: Lessons learned from 4 case studies. *Biologicals* **42**, 223–236 (2014).

10. Klug, B. *et al.* Adventitious agents and live viral vectored vaccines: Considerations for archiving samples of biological materials for retrospective analysis. *Vaccine* **34**, 6617–6625 (2016).

11. Victoria, J. G. *et al.* Viral Nucleic Acids in Live-Attenuated Vaccines: Detection of Minority Variants and an Adventitious Virus. *J. Virol.* **84**, 6033–6040 (2010).

12. Morris, C., Lee, Y. S. & Yoon, S. Adventitious agent detection methods in bio-pharmaceutical applications with a focus on viruses, bacteria, and mycoplasma. *Curr. Opin. Biotechnol.* **71**, 105–114 (2021).

13. Charlebois, R. L. *et al.* Sensitivity and breadth of detection of high-throughput sequencing for adventitious virus detection. *npj Vaccines* **5**, 61 (2020).

14. Onions, D. & Kolman, J. Massively parallel sequencing, a new method for detecting adventitious agents. *Biologicals* **38**, 377–380 (2010).

15. Mee, E. T. *et al.* Development of a candidate reference material for adventitious virus detection in vaccine and biologicals manufacturing by deep sequencing. *Vaccine* **34**, 2035–2043 (2016).

16. McClenahan, S. D., Uhlenhaut, C. & Krause, P. R. Evaluation of cells and biological reagents for adventitious agents using degenerate primer PCR and massively parallel sequencing. *Vaccine* **32**, 7115–7121 (2014).

17. Richards, B. *et al.* Detection of Adventitious Agents Using Next-Generation Sequencing. *PDA J. Pharm. Sci. Technol.* **68**, 651 LP – 660 (2014).

18. Kumar, D., Beach, N. M., Meng, X.-J. & Hegde, N. R. Use of PCR-based assays for the detection of the adventitious agent porcine circovirus type 1 (PCV1) in vaccines, and for confirming the identity of cell substrates and viruses used in vaccine production. *J. Virol. Methods* **179**, 201–211 (2012).

19. Flatschart, R. B. *et al.* Absolute quantification of Bovine Viral Diarrhea Virus ({BVDV}) {RNA} by the digital {PCR} technique. *J. Phys. Conf. Ser.* **575**, 12038 (2015).

20. Suo, T. *et al.* ddPCR: a more accurate tool for SARS-CoV-2 detection in low viral load specimens. *Emerg. Microbes |& Infect.* **9**, 1259–1268 (2020).

21. Kralik, P. & Ricchi, M. A Basic Guide to Real Time PCR in Microbial Diagnostics: Definitions, Parameters, and Everything . *Frontiers in Microbiology* vol. 8 (2017).

22. Taylor, S. C., Laperriere, G. & Germain, H. Droplet Digital PCR versus qPCR for gene expression analysis with low abundant targets: from variable nonsense to publication quality data. *Sci. Rep.* **7**, 2409 (2017).

23. Dantham, V. R. *et al.* Label-Free Detection of Single Protein Using a Nanoplasmonic-Photonic Hybrid Microcavity. *Nano Lett.* **13**, 3347–3351 (2013).

24. Young Hee Choi, and A.-M. Y. Single-Molecule Detection of Protein Efflux from Microorganisms using Fluorescent Single Walled Carbon Nanotube Sensor Arrays. *Physiol. Behav.* **176**, 139–148 (2019).

25. Squires, T. M., Messinger, R. J. & Manalis, S. R. Making it stick: Convection, reaction and diffusion in surface-based biosensors. *Nat. Biotechnol.* **26**, 417–426 (2008).

26. Wei, X., Panindre, P., Zhang, Q. & Song, Y. A. Increasing the Detection Sensitivity for DNA-Morpholino Hybridization in Sub-Nanomolar Regime by Enhancing the Surface Ion Conductance of PEDOT:PSS Membrane in a Microchannel. *ACS Sensors* **1**, 862–865 (2016).

27. Ouyang, W. & Han, J. Universal amplification-free molecular diagnostics by billion-fold hierarchical nanofluidic concentration. *Proc. Natl. Acad. Sci.* 201904513 (2019) doi:10.1073/pnas.1904513116.

28. Cheow, L. F., Ko, S. H., Kim, S. J., Kang, K. H. & Han, J. Increasing the Sensitivity of Enzyme-Linked Immunosorbent Assay Using Multiplexed Electrokinetic Concentrator. *Anal. Chem.* **82**, 3383–3388 (2010).

29. Berzina, B. & Anand, R. K. Continuous micellar electrokinetic focusing of neutral species driven by ion concentration polarization. *Lab Chip* **19**, 2233–2240 (2019).

30. Ouyang, W. *et al.* Microfluidic Platform for Assessment of Therapeutic Proteins Using Molecular Charge Modulation Enhanced Electrokinetic Concentration Assays. *Anal. Chem.* **88**, 9669–9677 (2016).

31. Kwak, R., Kim, S. J. & Han, J. Continuous-flow biomolecule and cell concentrator by ion concentration polarization. *Anal. Chem.* **83**, 7348–7355 (2011).

32. Berzina, B. & Anand, R. K. An Electrokinetic Separation Route to Source Dialysate from Excess Fluid in Blood. *Anal. Chem.* **90**, 3720–3726 (2018).

33. Kwon, H. J. *et al.* Comprehensive Electrokinetic-Assisted Separation of Oil Emulsion with Ultrahigh Flux. *ACS Nano* **15**, 15815–15823 (2021).

34. Volpatti, L. R. & Yetisen, A. K. Commercialization of microfluidic devices. *Trends Biotechnol.* **32**, 347–350 (2014).

35. Shakeri, A., Khan, S. & Didar, T. F. Conventional and emerging strategies for the fabrication and functionalization of PDMS-based microfluidic devices. *Lab Chip* **21**, 3053–3075 (2021).

36. Gale, B. K. *et al.* A review of current methods in microfluidic device fabrication and future commercialization prospects. *Inventions* **3**, (2018).

37. Jeon, H., Kwon, T., Yoon, J. & Han, J. Engineering a deformation-free plastic spiral inertial microfluidic system for CHO cell clarification in biomanufacturing. *Lab Chip* **22**, 272–285 (2022).

38. Martins, D., Levicky, R. & Song, Y.-A. Enhancing the speed of morpholino-DNA biosensor by electrokinetic concentration of DNA in a microfluidic chip. *Biosens. Bioelectron.* **72**, 87–94 (2015).

39. Ouyang, W., Li, Z. & Han, J. Pressure-Modulated Selective Electrokinetic Trapping for Direct Enrichment, Purification, and Detection of Nucleic Acids in Human Serum. *Anal. Chem.* **90**, 11366–11375 (2018).

40. Lee, S. *et al.* Nanoelectrokinetic bufferchannel-less radial preconcentrator and online extractor by tunable ion depletion layer. *Biomicrofluidics* **13**, (2019).

41. Dydek, E. V. *et al.* Overlimiting current in a microchannel. *Phys. Rev. Lett.* **107**, 1–5 (2011).

42. Davidson, S. M., Andersen, M. B. & Mani, A. Chaotic induced-charge electro-osmosis. *Phys.*

Rev. Lett. **112**, 1–5 (2013).

43. Chang, H. C., Yossifon, G. & Demekhin, E. A. Nanoscale electrokinetics and microvortices: How microhydrodynamics affects nanofluidic ion flux. *Annu. Rev. Fluid Mech.* **44**, 401–426 (2011).

44. Kim, K., Kim, W., Lee, H. & Kim, S. J. Stabilization of ion concentration polarization layer using micro fin structure for high-throughput applications. *Nanoscale* **9**, 3466–3475 (2017).

Chapter 2 Principles of Electrokinetic Concentration

A variety of electrokinetic phenomena are present in microfluidic concentration systems and the physics involved in those phenomena will be briefly explained here.

2.1 Electrokinetic Phenomena and Ion Transport

Conventionally, surface charge accumulation in hydrophilic materials such as glass is caused by pH-dependent ionization of functional surface groups (*e.g.,* silanes) and preferential adsorption of ions. Materials such as PDMS are actually charge neutral in the bulk and the mechanism of surface charge formation is still not well understood, but the electrokinetic phenomena at the surface are similar to those hydrophilic materials[1,2]. Counter-ions are attracted to the surface charges and form a charge distribution known as the electrical double layer (EDL)[3]. The EDL screens the effects of the surface charges so that no net electric field is experienced by ions in the bulk, and the length scale that describes this screening effect is the Debye length. The Debye length, seen in **Equation 2-1**, is determined by the permittivity (ε), Boltzmann constant (k_B), temperature (T), bulk concentration of each ionic species (c_i^0), and valency of each ionic species (z_i).

$$\lambda_D = \sqrt{\frac{\varepsilon k_B T}{e^2 \sum_i c_i^0 Z_i^2}} \tag{2-1}$$

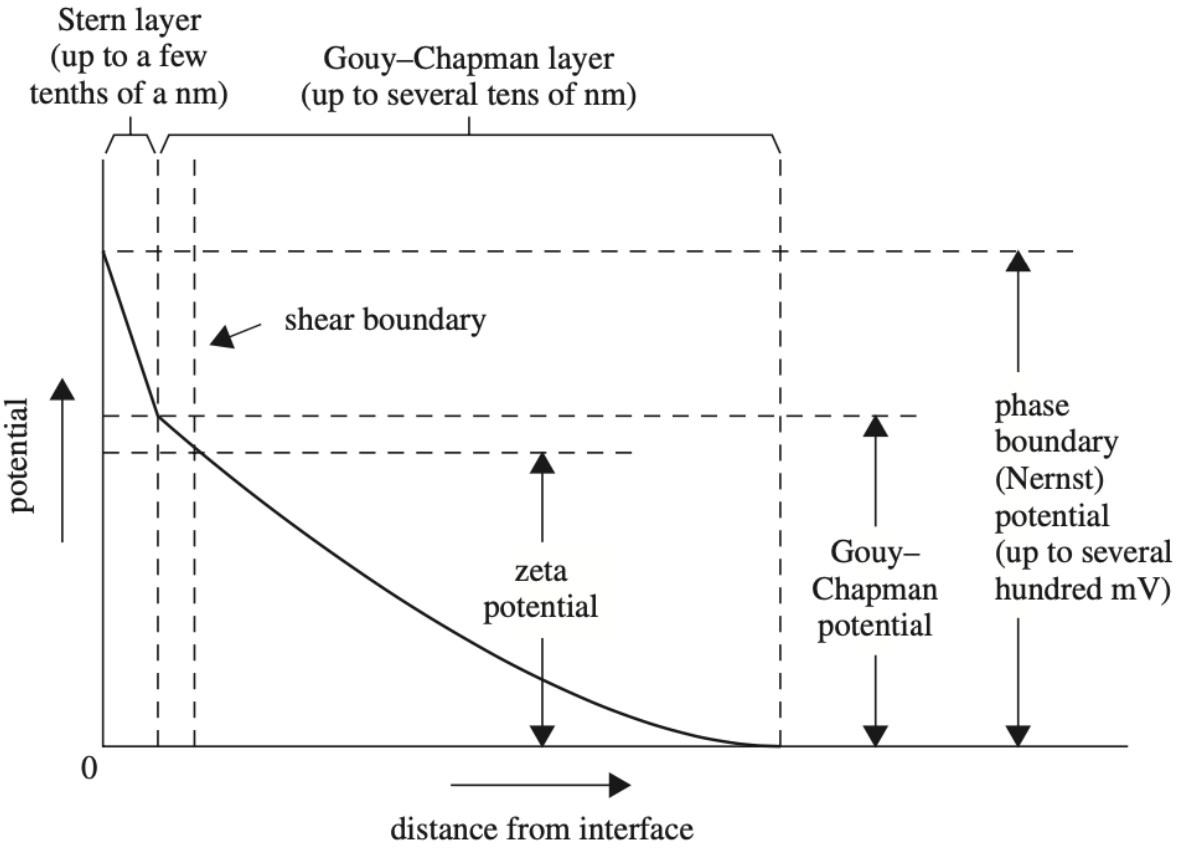

Figure 2-1 A diagram of the electrical double layer present on surfaces in a microfluidic device. The example shown in this diagram corresponds to a negative surface charge that accumulates positive ions in the double layer. Figure reproduced from *Fields, Forces, and Flows in Biological Systems*[4].

There are several models for the structure of the electrical double layer, but for explaining electroosmotic flow we will consider a thin layer of immobile charges adhered to the surface (The Stern Layer) and a diffuse layer of mobile charges (The Gouy-Chapman layer), illustrated in **Figure 2-1**. When an electric field is applied to a microchannel, the positive mobile ions in the double layer will flow from anode to cathode. The flow of ions in the double layer will effectively create a 'slipping' boundary condition that, through viscous coupling, will eventually create the plug flow profile seen in **Figure 2-2a**. The electric

potential of this slipping plane compared to the bulk (ground) is known as the zeta potential. In further detail, whether the boundary condition of the channel walls can actually be considered no-slip depends upon wetting properties of the material.[5] However, even in the case where stationary ions present in the Stern Layer cause a no-slip boundary at the edges of a channel, the transition from the bulk flow velocity to zero will happen within the distance of a few Debye Lengths from the wall. The velocity of the fully developed bulk flow, seen in **Equation 2-2**, depends upon the value of the zeta potential (ζ), applied electric field (E_0), permittivity of the fluid (ε), and viscosity of the fluid (μ).

$$U_{EOF} = \left(\frac{-\varepsilon\,\zeta}{\mu}\right)E_0 \tag{2-2}$$

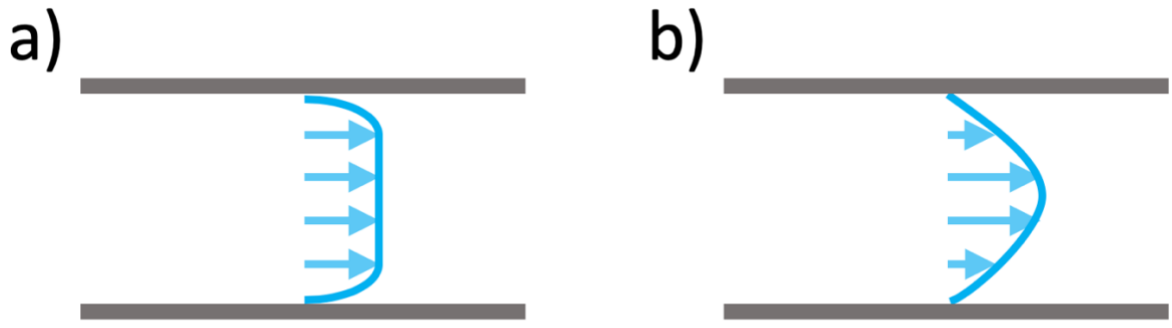

Figure 2-2 a) An illustration of the flow profile in a channel driven by electroosmotic flow. B) An illustration of flow profile typical for pressure driven laminar flow, the Poiseuille plug flow.

Convection of ions *via* fluid flow is just one mode of ion transport; diffusion and electrophoresis help complete the model of ion transport in a fluid. Concentration of ionic

species will be represented by c_i and the total molar flux will be represented by N. Fick's first law describes diffusive flux and can be seen in **Equation 2-3** in which D_i is the diffusion coefficient for the ionic species c_i.

$$N_{diffusion} = -D_i \nabla c_i \tag{2-3}$$

Conservation of mass requires that the change in concentration over time at a given location can only be cause by flux adding and removing particles, therefore **Equation 2-4** establishes the relationship between the change in concentration over time to the divergence of flux.

$$\frac{\partial c_i}{\partial \mathrm{t}} = -\nabla \cdot N_i \tag{2-4}$$

Taking the divergence of both sides of **Equation 2-3** and then combining it with **Equation 2-4** produces **Equation 2-5**, Fick's second law which establishes how concentration is affected by diffusion over time.

$$\frac{\partial c_i}{\partial \mathrm{t}} = D_i \nabla^2 c_i \tag{2-5}$$

Ion flux caused by electric fields, also known as electrophoresis, is described by **Equation 2-6** in which μ_i represents the electrophoretic mobility of a molecule and φ represents the electric potential. Using the same process as before we use **Equation 2-4** to and produce **Equation 2-7**.

$$N_{electrophoresis} = -\mu_i c_i \nabla \varphi \tag{2-6}$$

$$\frac{\partial c_i}{\partial \mathrm{t}} = \nabla \cdot (\mu_i c_i \nabla \varphi) \tag{2-7}$$

Finally, we describe the ionic flux and change in concentration over time caused by convection in **Equation 2-8** and **Equation 2-9** respectively where U represents the fluid velocity.

$$N_{convection} = Uc_i \tag{2-8}$$

$$\frac{\partial c_i}{\partial \mathrm{t}} = -\nabla \cdot (Uc_i) \tag{2-9}$$

Combining the all the types of flux to account all the modes of ionic transport in a system yields **Equation 2-10**, the Nernst-Planck Equation. This equation can quickly become complicated to solve. When electroosmotic flow is involved, U is coupled to the applied electric field and space charge distribution. In situations and time scales where charge neutrality is not guaranteed **Equation 2-10** must be coupled to the electrostatic Poisson equation to account for the forces charged ionic species exert on each other.[6]

$$\frac{\partial c_i}{\partial \mathrm{t}} = \nabla \cdot (D_i \nabla c_i - Uc_i + \mu_i c_i \nabla \varphi) \tag{2-10}$$

Previous EK concentrators have operated using a combination of pressure and electroosmotic flow. Our device described in the following chapter primarily uses pressure driven flow, but non-linear electroosmotic flow also causes instability in devices so it is important to understand the theory behind this phenomenon.

2.2 Ion Exchange Membrane

Ion exchange membranes (IEMs) are typically polymers that selectively transport a particular ionic species while acting as a barrier for fluid, and IEMs are a critical component of nearly every EK concentrator device. Generally, IEMs contain functional groups attached to a polymer backbone that become charged once the membrane absorbs a solvent such as water that causes ion dissociation.[7] The ionic functional groups give the membrane a fixed spatial charge that causes the formation of a potential at the surface of the membrane as ions move towards equilibrium. This potential, illustrated in **Figure 2-3**, is called the Donnan potential and creates the permselectivity of the IEM at equilibrium[8].

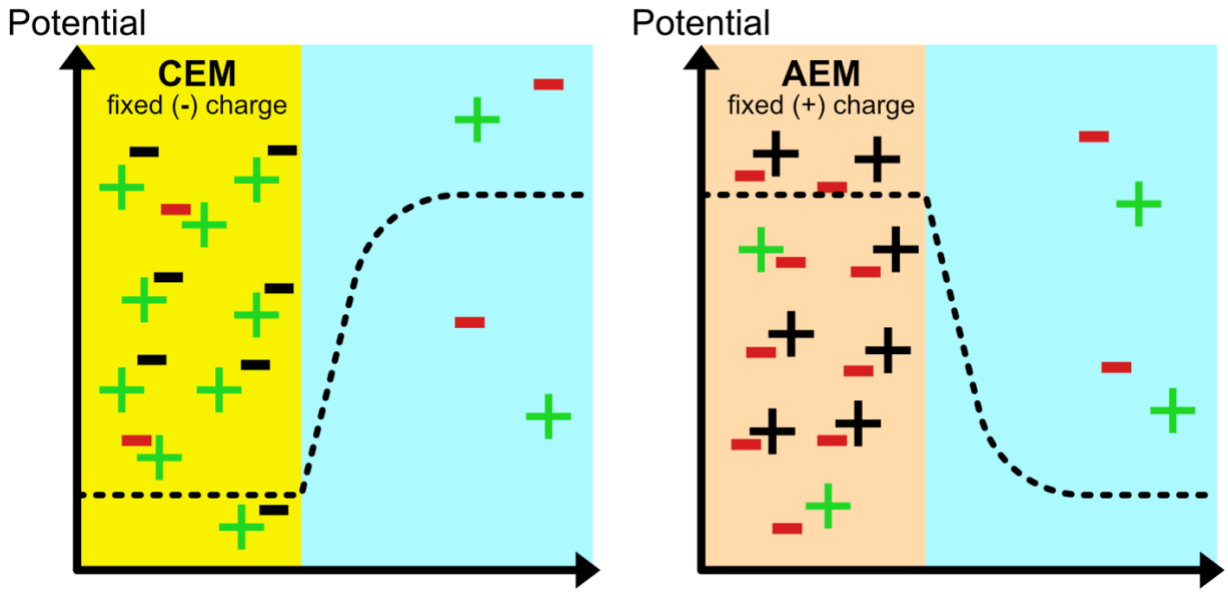

Figure 2-3 An illustration of the Donnan potential formed by each type of IEM. Charges depicted by colored symbols are mobile ions, black symbols represent immobile ions.

While analysis of the bulk IEM material and surrounding fluid is sufficient to explain the equilibrium behavior of the IEM, analysis of the inner IEM microstructure is needed to

explain the active transport of ions when a voltage bias is applied. The inner structure of IEMs and how they transport ions is still an active area of research, with questions not completely answered as to how the different phases present in a hydrated membrane affect ion tranport[7,9,10].

We will discuss the pore model often associated with the widely used CEM material, Nafion, which may not reflect the structure of Nafion exactly but does describe its transport behavior well[11,12]. In this model, the IEM can be thought of as an interconnected network of pores with fixed charges on the walls and water inside the pores. Ions are transported through the network via a combination of diffusion, electrophoretic migration, convection, and 'hopping' along surface charge sites. Illustrations of how ions are selectively transported when the membrane is biased can be seen in **Figure 2-4**. This model of ion transport is similar to how microfluidic nanochannels become ion selective because overlapping electrical double layers from the walls create a potential barrier that blocks co-ions[13].

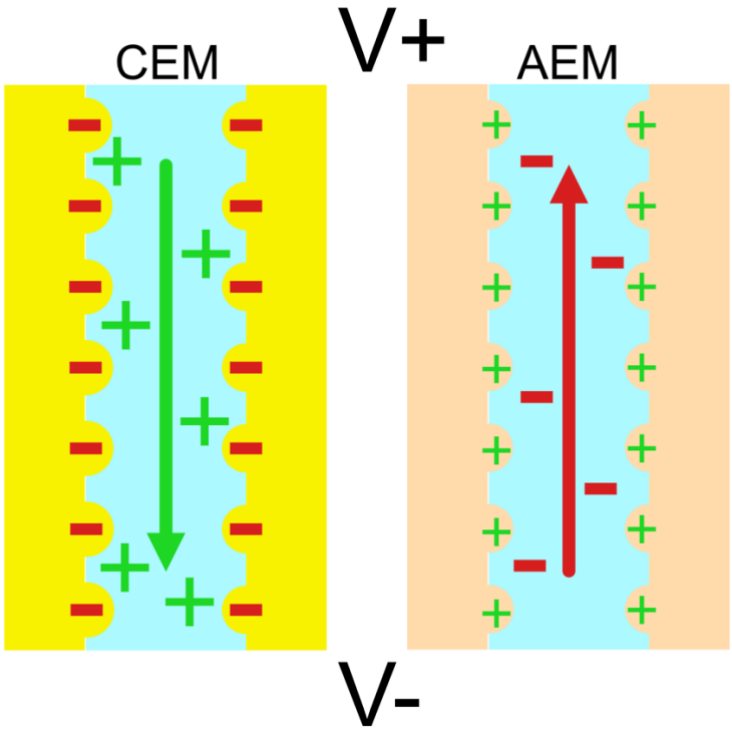

Figure 2-4 Illustrations of the microstructures formed by the different phases inside an IEM, and the ionic flux generated by an applied bias in a CEM & AEM respectively. Charges on the channel walls of the membrane are fixed while counter-ions are mobile.

2.3 Ion Concentration Polarization

The selective transport of ions made possible by IEMs gives rise to an important phenomenon that makes EK concentration possible, Ion Concentration Polarization (ICP). Applying a bias to an IEM creates a region depleted of ions on one side of the membrane and an enriched region on the other side, leading to ICP. Depending upon parameters such as the applied bias and flow, the ion depletion region can expand, as counter ions are removed by the membrane while co-ions migrate away from the membrane surface. The ion enrichment region is less relevant to the application of EK concentrators, and the enrichment side of the

membrane is often rinsed to prevent ion accumulation that would decrease the efficiency of the membrane extracting ions from the sample channel. The presence of the depletion region can be monitored by measuring the current in a device as a function of voltage. Initially current will increase linearly with voltage in the 'ohmic' regime, but eventually in the 'limiting' regime the depletion region will create a region of low conductivity in the device that will prevent further current increases.

During the ICP phenomenon there is an 'extended' electrical double layer near the membrane surface where additional space charges (co-ions) can accumulate near the membrane surface. This can lead to electroosmotic instability through generation of vortical flow[14–16]. Increasing the voltage applied to a device will eventually move it past the 'limiting' regime and into the 'overlimiting' regime, in which the non-linear electroosmotic flow near the membrane surface becomes significant. To prevent the vortices from growing and destabilizing the ICP zones it has been proven useful to add microstructures that confine the chaotic flow, and the device we propose in the next chapter makes use of this strategy[17].

2.4 Theoretical Model for EK Concentrator

Having explained the physics associated with ion transport and how IEMs can be used to locally alter the concentration of ions in a solution, we can now examine how an EK concentrator operates and some of the theoretical limits of performance. **Figure 2-5** shows an illustration of an EK concentrator that uses a CEM connecting two channels to generate a

depletion region via ICP. In this example device, negatively charged biomolecules are propelled by pressure-driven or electroosmotic flow and repelled by electrophoretic forces. To maintain the current continuity, the depletion region locally increases the magnitude of the electric field (to compensate for the reduced conductivity within the depletion region), thus locally increasing the electrophoretic force on the analyte and causing them to accumulate upstream of the depletion region.

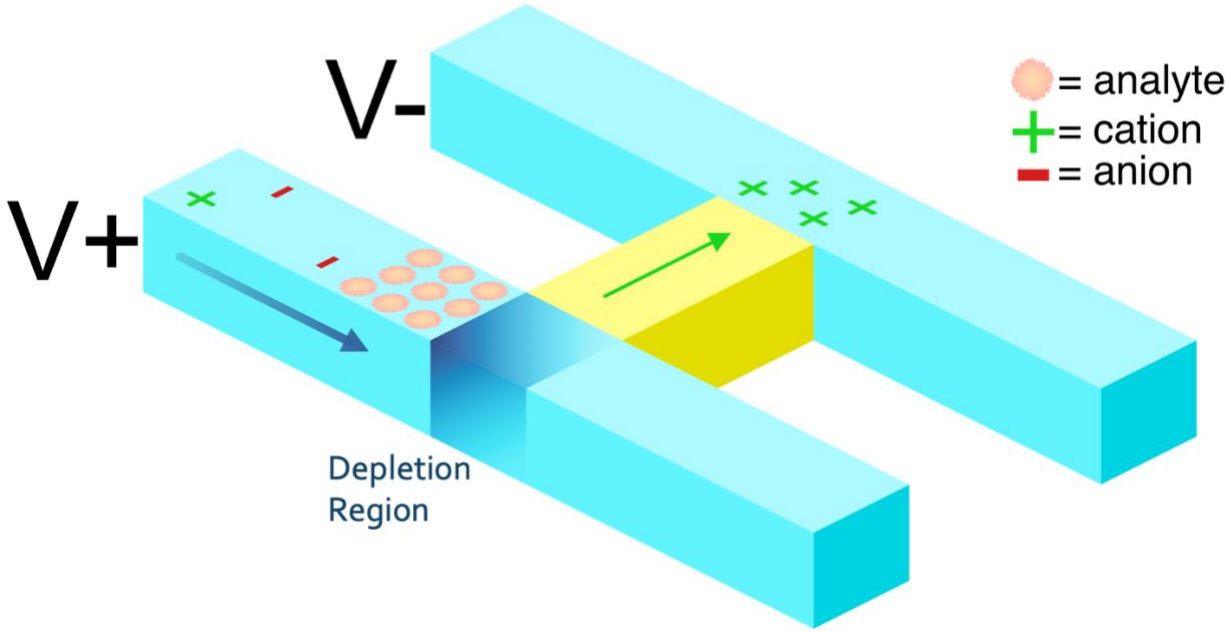

Figure 2-5 Illustration of an example EK concentrator that uses a CEM to bridge two separate channels.

An illustration of the forces acting on the molecules trapped by an EK concentrator can been in **Figure 2-6**. Neutral particles without net charge pass through the depletion region, propelled forward by fluid flow. Particles with negative net charge are trapped at the edge of the depletion region by the electrophoretic force. When comparing particles with similar mass the particles with greater negative charge—and therefore greater

electrophoretic mobility—accumulate even further upstream. It is worth noting in some systems there may be additional forces such as electroosmosis.

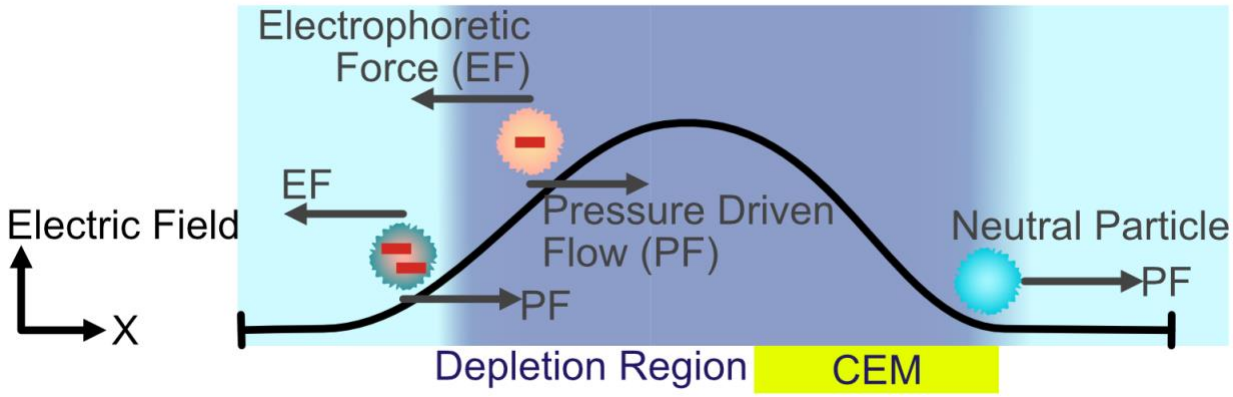

Figure 2-6 Illustration of forces acting on charged and uncharged molecules at the edge of the depletion region in a concentrator.

As previously mentioned, modeling EK concentrator systems to characterize their behavior has been a significant challenge due to the coupled equations and non-linear physics involved. However, in the past decade there has been significant progress in modeling that has yielded some fundamental insights about EK concentrator systems. For example, rotating vortices generated in the depletion region decrease pressure upstream in the device and decrease pressure downstream, leading to a fluid pumping effect[18]. In certain circumstances, it is even possible for this ICP pumping effect to contribute more to flow than electroosmosis. Simplified devices with a single CEM inside the channel have been analyzed to provide optimized dimensions for the channel and CEM, as well as optimized ionic buffer strength[20].

Importantly, it has been discovered that there are different operating regimes that limit the maximum concentration factor (CF) attainable by a given device[19]. The 'EK limit'

attainable when analytes are not effectively trapped is much smaller than the 'electroneutrality limit', in which the analyte completely replaces background (majority) ionic species. When discussing concentration performance of devices it is important to keep in mind the difference between *in situ* CF and the extracted sample CF. For devices in which analysis of the concentrated biomolecules will be done inside the channel it is possible to raise the CF by making the channel volume small. For example, in these devices concentrating a microliter of solution into a picoliter volume would produce a maximum *in situ* CF of a million-fold. In comparison, if the concentrated biomolecules are to be extracted from the device for analysis then the maximum CF is the input sample volume divided by the extracted volume. Therefore a device with a high *in situ* CF could produce a low extraction CF if the sample throughput is not large compared to the extraction volume.

2.5 References

1. Wheeler, A. R., Trapp, G., Trapp, O. & Zare, R. N. Electroosmotic flow in a poly(dimethylsiloxane) channel does not depend on percent curing agent. *Electrophoresis* **25**, 1120–1124 (2004).
2. Tandon, V., Bhagavatula, S. K., Nelson, W. C. & Kirby, B. J. Zeta potential and electroosmotic mobility in microfluidic devices fabricated from hydrophobic polymers: 1. The origins of charge. *Electrophoresis* **29**, 1092–1101 (2008).
3. Butt, H. J., Graf, K. & Kappl, M. Chapter 4. The Electric Double Layer. *Phys. Chem. interfaces* (2003).
4. Grodzinksy, A. J. *Fields, Forces, and Flows in Biological Systems*.
5. Joly, L., Ybert, C., Trizac, E. & Bocquet, L. Hydrodynamics within the electric double layer on slipping surfaces. *Phys. Rev. Lett.* **93**, 1–4 (2004).
6. Lu, B., Holst, M. J., Andrew McCammon, J. & Zhou, Y. C. Poisson–Nernst–Planck equations for simulating biomolecular diffusion–reaction processes I: Finite element solutions. *J. Comput. Phys.* **229**, 6979–6994 (2010).
7. Luo, T., Abdu, S. & Wessling, M. Selectivity of ion exchange membranes: A review. *J. Memb. Sci.* **555**, 429–454 (2018).
8. Donnan, F. G. The theory of membrane equilibria. *Chem. Rev.* **1**, 73–90 (1924).
9. Mauritz, K. A. & Moore, R. B. State of Understanding of Nafion. *Chem. Rev.* **104**, 4535–4586 (2004).
10. Ariono, D., Khoiruddin, Subagjo & Wenten, I. G. Heterogeneous structure and its effect on properties and electrochemical behavior of ion-exchange membrane. *Mater. Res. Express* **4**, 24006 (2017).
11. Paddison, S. J. & Paul, R. The nature of proton transport in fully hydrated Nafion®. *Phys. Chem. Chem. Phys.* **4**, 1158–1163 (2002).
12. Cwirko, E. H. & Carbonell, R. G. Interpretation of transport coefficients in Nafion using a parallel pore model. *J. Memb. Sci.* **67**, 227–247 (1992).
13. Wang, Y. C. & Han, J. Pre-binding dynamic range and sensitivity enhancement for immuno-sensors using nanofluidic preconcentrator. *Lab Chip* **8**, 392–394 (2008).
14. Druzgalski, C. L., Andersen, M. B. & Mani, A. Direct numerical simulation of electroconvective instability and hydrodynamic chaos near an ion-selective surface. *Phys. Fluids* **25**, (2013).
15. De Valença, J. C., Wagterveld, R. M., Lammertink, R. G. H. & Tsai, P. A. Dynamics of microvortices induced by ion concentration polarization. *Phys. Rev. E - Stat. Nonlinear, Soft Matter Phys.* **92**, 1–5 (2015).
16. Kwak, R., Lim, K. M., Han, J. & others. Shear flow of an electrically charged fluid by ion concentration polarization: Scaling laws for electroconvective vortices. *Phys. Rev. Lett.* **110**, 114501 (2013).
17. Kim, K., Kim, W., Lee, H. & Kim, S. J. Stabilization of ion concentration polarization layer using micro fin structure for high-throughput applications. *Nanoscale* **9**, 3466–

3475 (2017).
18. Li, Z. *et al.* Accurate Multi-Physics Numerical Analysis of Particle Preconcentration Based on Ion Concentration Polarization. *Int. J. Appl. Mech.* **9**, 1–21 (2017).
19. Ouyang, W., Ye, X., Li, Z. & Han, J. Deciphering ion concentration polarization-based electrokinetic molecular concentration at the micro-nanofluidic interface: theoretical limits and scaling laws. *Nanoscale* **10**, 15187–15194 (2018).
20. Jia, M. & Kim, T. Multiphysics simulation of ion concentration polarization induced by a surface-patterned nanoporous membrane in single channel devices. *Anal. Chem.* **86**, 10365–10372 (2014).

Chapter 3. Methods and Materials for building EK Concentrators

In this chapter we review prior EK concentrator designs and compare their advantages with respect to concentration performance and manufacturability. We then propose a low-cost EK concentrator design and describe the materials and processes used to manufacture it.

3.1 Previous Concentrator Designs

Over the past two decades a variety of EK concentrator designs have been explored, and some noteworthy examples are described in **Table 3-1**. The first concentrators did not involve a polymer ion exchange membrane, and instead utilized the ion selective properties of glass nanochannels [1–3]. Similar to how Nafion is cation-selective due to its nano-porous structure and fixed negative charges, glass nanochannels are cation-selective due to the negative surface charges on the glass walls. The advantage of glass nanochannel concentrators is the fact that it does not need an IEM to be incorporated into a standard MEMS fabrication. However, there is a drawback in the precision needed for the glass etch lithography, and nanochannels generally have low current throughput limiting their performance as IEMs.

Other EK concentrators make use of one or more IEMs to generate the ICP phenomena. A general schematic of the most commonly-used concentrator design can be seen in **Figure 3-1**, in which a single Cation Exchange Membrane (CEM) is placed inside a microfluidic channel. This design is favorable and simple because electrodes can be placed

directly into the sample channel and a single voltage bias will drive electroosmotic flow and generate the depletion region at the same time.

Devices driven by electroosmotic flow alone have a comparatively low flowrate, and thus parallel microchannels in combination with pressure-driven flow have been a common strategy to increase the sample throughput of devices[4,5]. These devices increase the effective device throughput but keep the individual channel sizes small near the membrane, where confinement of vortices is needed.

Some researchers have begun to explore designs and materials that are different from the typical planar microfluidic chip. Paper EK concentrators make use of the microporous structure of filter paper to effectively create a 3D network of microchannels, and may be able to improve the sensitivity of lateral flow assays in a point-of-care setting[6–8]. Other devices have made use of 3D printed parts with microporous structures inside the main channel[9]. These devices offer a point of inspiration for our proposed design, where the actual channel dimensions are much larger than previous EK concentrators, but the microporous structure inside the channel decreases the effective channel size near the IEM.

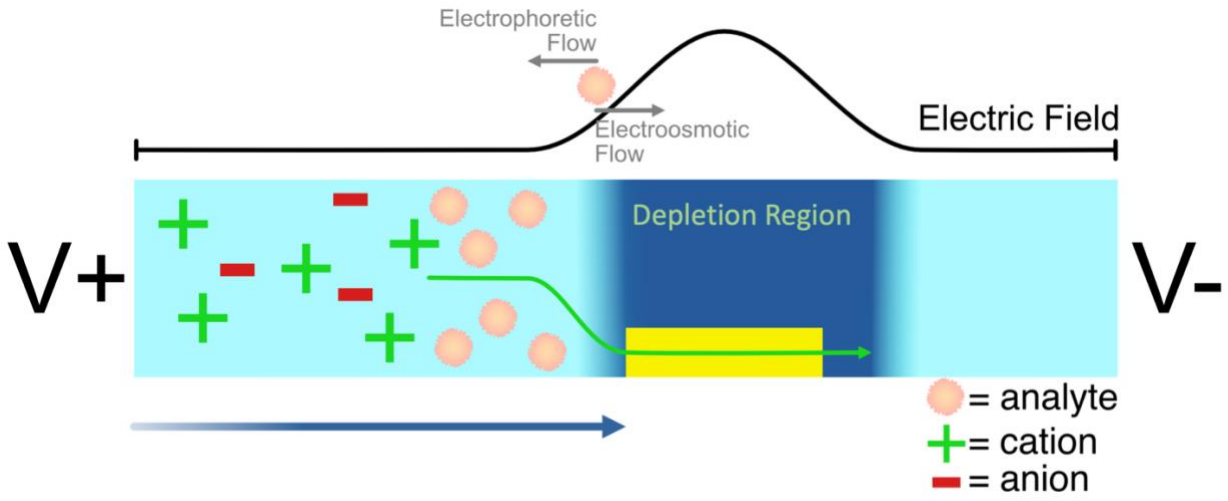

Figure 3-1 High level schematic of single in-channel CEM device.

Table 3-1

Device Type	Advantages	Disadvantages	References
Hierarchical Concentrator	+ Billion-fold enrichment + High throughput + Selective enrichment	- High manufacturing complexity when stacking - High operational complexity	4
Hybrid EK Filter	+ Very high throughput + Adaptable to different sample volumes	- Difficult sample extraction	5
Bifurcated Nafion Junction	+ Stable depletion zone with high ionic strength buffer + Concentrates whole RBC's	- Low throughput - Careful Nafion alignment required	6,7
Radial Flow Concentrator	+ Easy sample extraction using pipette tips	- Difficult to adapt to highly parallel design	8
Single Channel PEDOT:PSS	+ Faster peak enrichment performance than Nafion + Greater flexibility in choosing membrane dimensions	- Careful alignment of membrane and channel	9,10
Paper based analytic devices (μPADs)	+ Simple and inexpensive to manufacture and operate + Easy to integrate with certain assays/sensors	- Difficult sample extraction - Difficult to control Nafion patterning - Inconsistent flow rate	11–14
Nanofluidic Channels	+ No ion selective membrane needed	- Low throughput - Tradeoff between nanochannel dimensions and manufacturing complexity	1–3
Heterogenous Junction	+ Stable depletion zone with high ionic strength buffer + Could be configured to concentrate anions	- Added manufacturing complexity from multiple hydrogels	15

3.2 Improved Materials

Polydimethylsiloxane (PDMS) is a polymer that has been popular in prototyping many types of microfluidic devices, including EK concentrators[4,6,16]. PDMS has been an ideal material for microfluidic research because it is low-cost, biocompatible, transparent, and easily moldable. Despite these useful properties, PDMS is not a popular choice for commercial microfluidic devices, with most companies choosing to use other polymers for their microfluidic chips. The surface of PDMS is hydrophobic and porous which can lead to significant absorption of hydrophobic small molecules[17]. Active research is being done on hydrophilic surface modification for PDMS, but this step would add manufacturing complexity and cost[18]. Additionally, the fabrication process for PDMS is complicated and expensive when compared to the injection molding or milling processes that can be used for many plastics.

Liquid Nafion resin has been commonly used by previous EK concentrators and was a good choice for rapid prototyping due to its ability to be patterned on a glass surface using a removable microchannel[19–21]. However, it has been shown previously that surface patterned Nafion can have relatively large variations in thickness[22]. For a device with Nafion resin in the channel the thickness could affect the device's performance in two ways that would lead to issues with reproducibility. A thinner Nafion membrane would leave more space between the channel walls and the membrane, affecting the critical channel dimension in the area meant to confine non-linear electroosmotic flow. Additionally, a thinner Nafion membrane

would lead to smaller portion of the channel with high cation conductivity. Variances in the channel dimension and ionic conductivity could cause identical operating parameters—such as voltage bias and pressure driven flow—to produce different results across devices. Nafion resin also has long-term issues with adhesion to glass slide substrates that lead to a failure during device operation.

To improve the reproducibility of EK concentrators, it would be ideal to use a commercially available solid ion exchange membrane, similar to those used for fuel cells and electrodialysis. Solid membranes would have better mechanical durability, reproducible ionic conductivity, and would allow diverse ion exchange membranes—such as anion exchange membranes—to be incorporated into devices. Solid Nafion membranes have already been incorporated into a PDMS EK concentrator.[23] However, the process for creating a properly sealed IEM junction required spin coating of PDMS onto the substrate to match the Nafion thickness, and careful alignment of the Nafion with microfluidic channel. Therefore, it would be ideal to find a simpler method for creating a junction between the channel and IEM so that the benefits of the solid membrane could be fully utilized.

3.3 Device Design

A schematic of the proposed manufacturable preconcentration device can be seen in **Figure 3-2**. The device consists of a main channel that a sample, containing a biomolecule with net charge in an ionic buffer solution, will pass through. Pressure-driven flow moves

the sample through the main channel as opposed to the electroosmotic flow used by previous devices. Using pressure driven flow allows for higher flowrates and decouples the flowrate from the membrane bias, allowing individual adjustment of the propulsive and repulsive forces acting on the molecules being concentrated.

Two separate 'membrane rinsing' channels sit above the main channel, with a fluid barrier provided by two cation exchange membranes (CEMs). The CEMs prevent mixing of the fluids in the rinsing channels and main channel but do allow for cations to pass from one channel to another. Electrodes in the rinsing channels bias the CEMs allowing the device to be operated without an electrode in the main channel. This electrode placement is preferable compared to previous devices because electrochemical reactions that occur near the electrode surface could lead to bubble generation or degradation of the sample. The device is biased such that the sample flows past the higher-voltage enriching membrane first and past the lower-voltage depleting membrane second. The membrane rinsing channels are continuously flushed with a buffer solution with the same ionic strength as the sample fluid.

A large reservoir of buffer solution flows through the rinsing channels at a sufficiently high flowrate such that there is no significant enrichment or depletion of ions near the membrane surface that faces the rinsing channels. Enrichment or depletion of ions near the membrane surface could decrease the efficiency of the membranes in removing or adding ions to the main channel, and therefore negatively impact device stability. Keeping the ionic strength of the solution in the rinse channels and near the membrane surfaces

constant allows the system to eventually reach a non-equilibrium steady state in which the current and depletion region are stable.

When the device is properly biased cations are removed from the main channel near the downstream CEM and a depletion region begins to form upstream of that membrane. The size and stability of the depletion region is dependent upon the applied bias, flowrate, and ionic buffer strength. With a sufficiently low flowrate, low ionic buffer strength, high voltage bias, or short channel it is possible for the depletion region to extend all the way upstream to the first CEM. If the depletion region reached the upstream CEM the voltage difference would extract cations from the rinse channel and therefore enrich the concentration of cations near the membrane in the main channel. This means the device dimensions and operating parameters can be adjusted such that the depletion region is contained between the two CEMs, therefore the device is theoretically more stable than the single CEM systems where the depletion region is able to extend upstream and become diffuse.

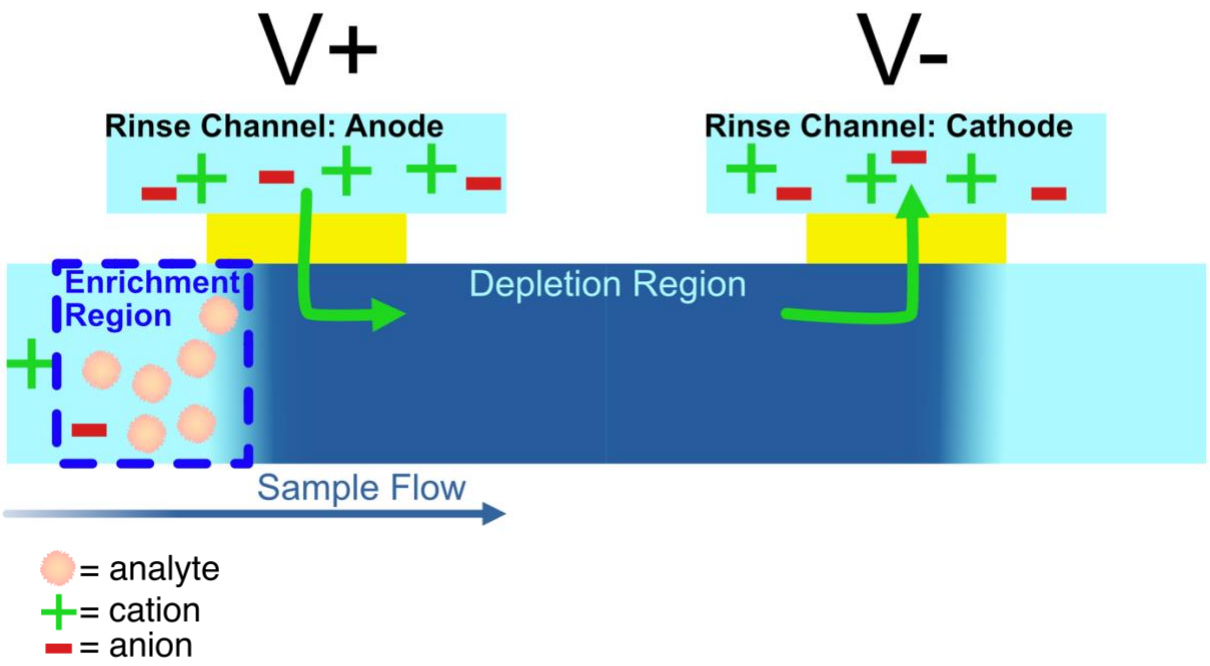

Figure 3-2 High level schematic of the dual-CEM concentration device.

A detailed diagram of the device can be seen in **Figure 3-3**. The substrate of the of the main channel is a piece of PMMA (OPTIX 0.093 in. Acrylic Sheet) that measures 137.5 mm by 25 mm. The main channel layer, IEM junction layer, and CEM gaskets are made of stacks of adhesive and polyethylene terephthalate (PTE) plastic. The stacks are formed by placing 1 mil thick PET film on a flat working surface and carefully rolling the 2 mil thick acrylic adhesive (3M465) onto each side, using a squeegee to flatten and remove any bubbles. A CO_2 laser cutter (Universal Laser Systems VLS6.75 75 Watt CO_2) was used to remove sections of the plastic-adhesive stacks to form a cutout for the main channel, holes in the IEM junction layer, and CEM gaskets. The holes in the IEM junction layer act as inlets and outlets to the main channel and expose small sections of the main channel to the CEMs. The main channel

is 1.5 mm wide by 112.5 mm long, and the holes for the IEM junction measure 5 mm by 5 mm.

The CO_2 laser was used to etch channels and cut inlets & outlets into pieces of acrylic measuring 25 mm by 25 mm, forming the membrane rinsing chips. A coarse rigid plastic mesh (50 x 50 Nylon 0.0085" wire diameter) was placed inside the rinsing channel to provide mechanical support to the membrane and prevent it from bending away from the main channel as the pressure in the channel increases. The depth of the rinsing channel was measured using a profilometer (Bruker DektakXT) to be 462 ± 14 μm. This channel depth was chosen to accommodate the support mesh.

The main channel and holes in the IEM junction are filled with layers of a microporous plastic mesh (Component Supply Company Nylon Mesh). The depth and width of channels in previous EK concentrators was typically on the order of tens of microns because smaller channel dimensions are better for stabilizing the non-linear electroosmotic flow that occurs at the IEM surface and in the depletion region. Our device is able to use much wider and deeper channels than previous devices because the microporous mesh in the channel is also able to limit the destabilizing effect of the vortices generated by the non-linear electroosmotic flow. The lateral dimensions of the mesh pieces are currently the limiting factor of the system dimensions, because mesh pieces cut smaller than 1.5 mm are heavily deformed by the heat produced during laser cutting and therefore unable to fit properly in the channel.

The device is assembled by aligning the various layers and applying pressure to make even contact with the adhesive layers. The Nafion membranes (Nafion 117) used for the CEMs swell when exposed to solvents, consequently they are placed in buffer solution of identical ionic strength to the solution that will be concentrated for at least 48 hours before use. The membranes are dried immediately before assembly in order to provide a dry surface for the adhesive to contact. The main channel and rinse channels are filled with buffer solution immediately after assembly and when the device is not in use. Keeping the device filled is to prevent the membranes from drying out because the deformation of the dry membranes could create leakage.

Thicknesses of the materials involved—seen in **Table 3-2**—were measured using a profilometer by attaching pieces to glass slides and taking measurements at five points 100 microns apart. This table also contains the costs associated with the materials involved and allows us to estimate the cost of a single device to be approximately $13, with 84% of the cost coming from the ion exchange membranes.

Table 3-2

Material	Thickness	Bulk Cost	Per Device Cost
7 Micron Pore Nylon Mesh (Component Supply Company)	53.503 ± 4.296 µm	$93.24 (18" x 20")	$0.12
18 Micron Pore Nylon Mesh (Component Supply Company)	70.461 ± 6.809 µm	$56.81 (18" x 20")	$0.07
35 Micron Pore Nylon Mesh (Component Supply Company)	66.923 ± 3.111 µm	$37.82 (18" x 20")	$0.05
2mil Adhesive/1mil PET-/2mil AdhesiveStack (Uline & McMaster-Carr)	125.977 ± 1.861 µm	3M 465 - $78.00 (3"x180') PET -$12.72 (40" x 10')	$0.07
Acryllic Sheet – 1/8" (OPTIX)	Not Measured	$49.28 (12" x 12")	$1.75
Nafion 117 (Fuel Cell Store)	Not Measured	$33.00 (10cm x 10cm)	$10.93

Total
$12.99

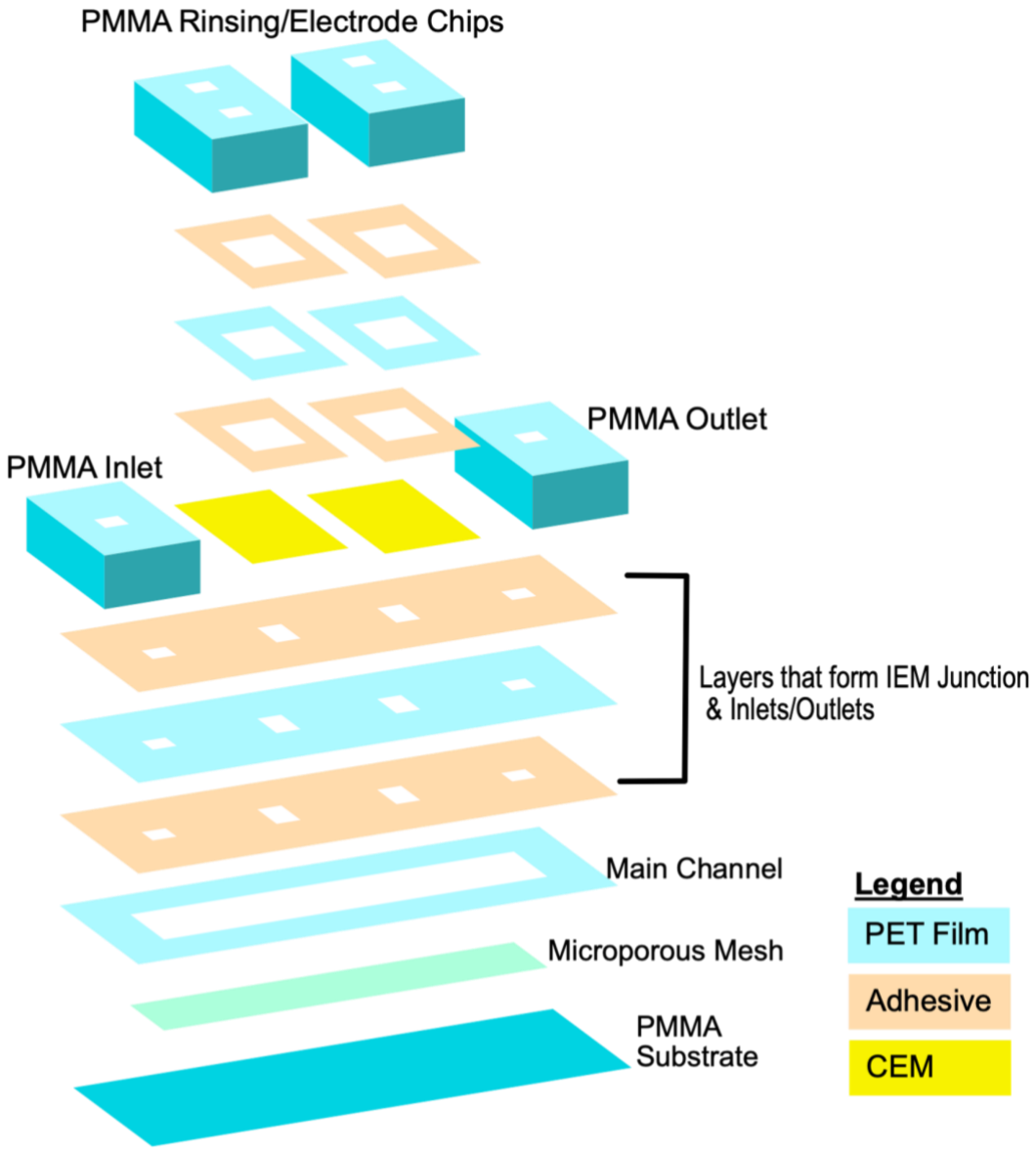

Figure 3-3 A diagram of the highly manufacturable concentrator.

3.4 References

1. Huang, K. Da & Yang, R. J. A nanochannel-based concentrator utilizing the concentration polarization effect. *Electrophoresis* **29**, 4862–4870 (2008).
2. Wang, Y. C., Stevens, A. L. & Han, J. Million-fold preconcentration of proteins and peptides by nanofluidic filter. *Anal. Chem.* **77**, 4293–4299 (2005).
3. Wang, Y. C. & Han, J. Pre-binding dynamic range and sensitivity enhancement for immuno-sensors using nanofluidic preconcentrator. *Lab Chip* **8**, 392–394 (2008).
4. Ouyang, W. & Han, J. Universal amplification-free molecular diagnostics by billion-fold hierarchical nanofluidic concentration. *Proc. Natl. Acad. Sci.* 201904513 (2019) doi:10.1073/pnas.1904513116.
5. Kwon, H. J. *et al.* Comprehensive Electrokinetic-Assisted Separation of Oil Emulsion with Ultrahigh Flux. *ACS Nano* **15**, 15815–15823 (2021).
6. Kim, J., Cho, I., Lee, H. & Kim, S. J. Ion Concentration Polarization by Bifurcated Current Path. *Sci. Rep.* **7**, 1–12 (2017).
7. Kwak, R., Kim, S. J. & Han, J. Continuous-flow biomolecule and cell concentrator by ion concentration polarization. *Anal. Chem.* **83**, 7348–7355 (2011).
8. Lee, S. *et al.* Nanoelectrokinetic bufferchannel-less radial preconcentrator and online extractor by tunable ion depletion layer. *Biomicrofluidics* **13**, (2019).
9. Wei, X., Panindre, P., Zhang, Q. & Song, Y. A. Increasing the Detection Sensitivity for DNA-Morpholino Hybridization in Sub-Nanomolar Regime by Enhancing the Surface Ion Conductance of PEDOT:PSS Membrane in a Microchannel. *ACS Sensors* **1**, 862–865 (2016).
10. Wei, X., Do, V. Q., Pham, S. V., Martins, D. & Song, Y. A. A Multiwell-Based Detection Platform with Integrated PDMS Concentrators for Rapid Multiplexed Enzymatic Assays. *Sci. Rep.* **8**, 1–11 (2018).
11. Han, S. Il, Hwang, K. S., Kwak, R. & Lee, J. H. Microfluidic paper-based biomolecule preconcentrator based on ion concentration polarization. *Lab Chip* **16**, 2219–2227 (2016).
12. Gong, M. M., Zhang, P., Macdonald, B. D. & Sinton, D. Nanoporous membranes enable concentration and transport in fully wet paper-based assays. *Anal. Chem.* **86**, 8090–8097 (2014).
13. Yang, R. J., Pu, H. H. & Wang, H. L. Ion concentration polarization on paper-based microfluidic devices and its application to preconcentrate dilute sample solutions. *Biomicrofluidics* **9**, 1–11 (2015).
14. Han, S. Il *et al.* High-ionic-strength pre-concentration via ion concentration polarization for blood-based biofluids. *Sensors Actuators, B Chem.* **268**, 485–493 (2018).
15. Kim, P., Kim, S. J., Han, J. & Suh, K. Y. Stabilization of ion concentration polarization using a heterogeneous nanoporous junction. *Nano Lett.* **10**, 16–23 (2010).
16. Xia, Y. & Whitesides, G. M. Soft lithography. *Angew. Chemie - Int. Ed.* **37**, 550–575 (1998).
17. Toepke, M. W. & Beebe, D. J. PDMS absorption of small molecules and consequences in microfluidic applications. *Lab Chip* **6**, 1484–1486 (2006).
18. Almutairi, Z., Ren, C. L. & Simon, L. Evaluation of polydimethylsiloxane (PDMS) surface modification approaches for microfluidic applications. *Colloids Surfaces A Physicochem. Eng. Asp.* **415**, 406–412 (2012).

19. Ko, S. H. *et al.* Nanofluidic preconcentration device in a straight microchannel using ion concentration polarization. *Lab Chip* **12**, 4472–4482 (2012).
20. Lee, J. H., Song, Y. A. & Han, J. Multiplexed proteomic sample preconcentration device using surface-patterned ion-selective membrane. *Lab Chip* **8**, 596–601 (2008).
21. Kwak, R., Kim, S. J. & Han, J. Continuous-flow biomolecule concentrator by ion concentration polarization. *14th Int. Conf. Miniaturized Syst. Chem. Life Sci. 2010, MicroTAS 2010* **2**, 887–889 (2010).
22. Kim, M., Jia, M. & Kim, T. Ion concentration polarization in a single and open microchannel induced by a surface-patterned perm-selective film. *Analyst* **138**, 1370–1378 (2013).
23. Phan, D. T., Yang, C. & Nguyen, N. T. Fabrication of nanoporous junctions using off-the-shelf Nafion membrane. *J. Micromechanics Microengineering* **25**, (2015).

Chapter 4. Validation and Optimization

Here we validate the concentrator design proposed in the previous chapter, and confirm our assumption about the ability of microporous mesh to stabilize EK concentration by testing several different meshes. We also explore how the concentration performance relates to the flow rate and voltage bias used to operate the device.

4.1 Experimental Setup

A photo of the experimental setup can be seen in **Figure 4-1,** and a labeled photo of the device can be seen in **Figure 4-2**. A syringe pump was used to pump the sample liquid through the device. A small syringe (3mL BD Plastipak) was used to minimize the disruptions to flow caused by the stepper motor of the pump when using low flowrates. Sample volumes were on the scale of hundreds of microliters, but dead volume with air pockets in the syringe and tubing had to be minimized because compressed air would cause deviations from the desired flowrate. Before withdrawing the sample solution into the pump tubing, the syringe and tubing were first filled with buffer solution and 50 microliters of air were withdrawn into the tubing to create a small space between the sample liquid and buffer. Two brushless motor pumps (DC 12V Micro Brushless Pump) were placed in a liter of buffer solution and connected to the membrane rinsing channels. The fluidic resistance of the tubing and rinsing channels led to a flowrate of 1 milliliter per minute at the highest power setting.

To apply voltage bias and measure current, a source meter (Keithley 2400) was used with LabVIEW software to record data automatically. When biasing the device, the voltage was raised from zero volts to the final value at a rate of 1 V/s to minimize the generation of turbulent electroosmotic flow near the downstream membrane. Electrodes (sintered Ag/AgCl A-M Systems) were threaded through small slits that were cut into tubing connected to the membrane rinsing channels, and held in place by UV cure epoxy (Loctite 352) that re-sealed the tubing.

Microscope images were collected and analyzed using ImageJ software and a CCD camera (SensiCam QE). Images of the area directly upstream of the depleting CEM were taken every minute while the device was being operated. Exposure times of 100ms, 10ms, and 1ms were used to image the concentration plug with exposure time being decreased when the cameras sensors became saturated. When comparing fluorescence intensity of images with different exposure times the values were weighted by dividing 100 by their exposure time. For example, fluorescence intensity values in an image taken with 100ms exposure were multiplied by a weight of 1, while values in an image take with an exposure of 10ms were multiplied by 10. For a given experimental run to calculate the concentration factor the peak fluorescence intensity value in the channel of the final image was divided by the peak value from the initial image.

The biomolecule used to measure concentration performance was a single strand DNA (SSDNA) (5'-GTA GGC GAA CCC TGC CCA GGT-3') tagged with Alexa Fluor 647.

Varying concentrations of the ssDNA in 0.1X phosphate buffered saline (PBS) solution were created using serial dilution.

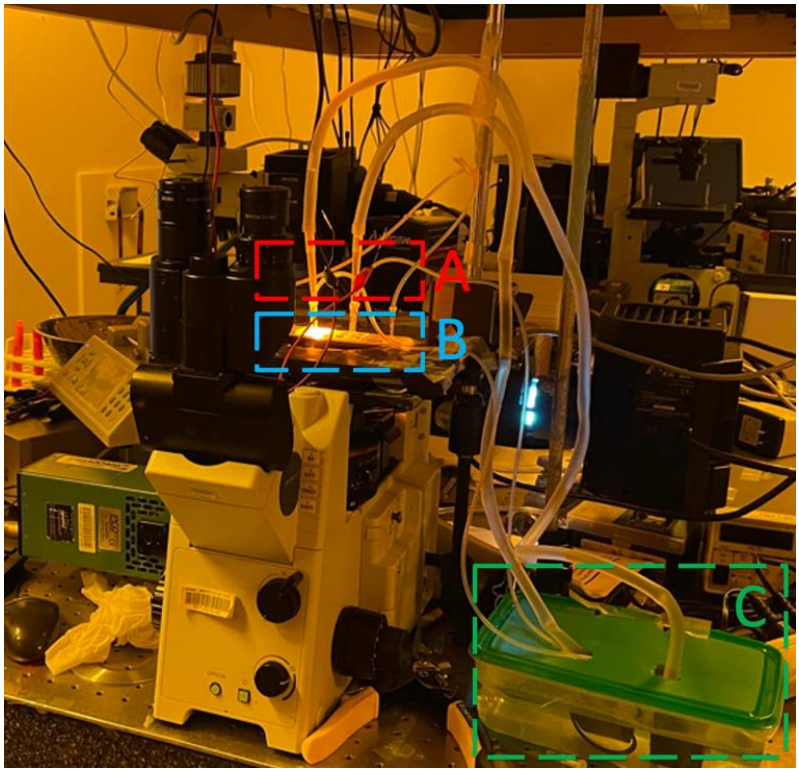

Figure 4-1 A labeled photograph of the experimental setup. The box labeled **A** shows the electrode-tubing assembly. The box labeled **B** contains the EK concentrator device. The box labeled **C** shows the rinsing pumps and buffer reservoir.

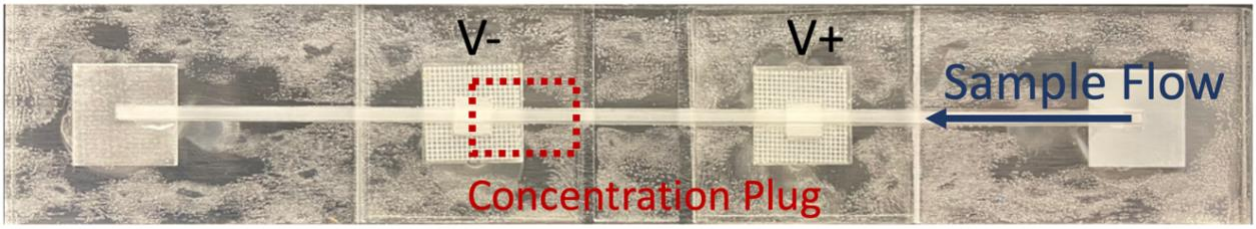

Figure 4-2 A labeled photograph of a device. The membrane labeled **V-** is the downstream depleting CEM while the membrane labeled **V+** is the upstream enriching CEM. The red dotted box shows the area of the channel where the concentration plug begins to form before expanding upstream in the channel.

4.2 Initial Validation of Concentration

Initially the device was operated at a low flowrate and relatively high voltage bias similar to previous EK concentrators from the literature. A flowrate of 0.8 microliters per minute and bias of 160V were used. Solution of ssDNA at 10 pM, 1 nM, and 100 nM concentrations were used to observe the formation and movement of a concentration plug and to measure the concentration factor. The pore size for the initial device was 18 microns.

The formation of a stable concentration plug can be seen in **Figure 4-3.** Initially the fluorescence intensity of the 1 nM fluorescently tagged ssDNA is too low to be seen against the background signal using 10 ms exposure time. After 30 minutes enough DNA has accumulated to become visible in a concentration plug that forms a thin band across the channel. Similar to previous EK concentrators where the plug meets the channel walls there is some leakage due to electroosmotic flow. Eventually after 150 minutes the depletion region has expanded slightly upstream, and ssDNA has continued to accumulate leading to 'stacking' of the analyte and expansion of the concentration plug.

All three concentrations of ssDNA tested became visible to the microscope after 30 minutes as shown in **Figure 4-4**, and the increase in fluorescence intensity can be seen in **Figure 4-5.** For the initial concentration of 100 nM a peak fluorescence intensity increase of 542 times was achieved in 30 minutes. This concentration factor (CF) is lower than values achieved by other EK concentrators with lower flowrates because the channel is larger and therefore the concentration plug is more dilute. However, the lower CF value is not a

disadvantage for this device because the eventual goal for this device is to extract the concentrated molecules. The current volume of concentration plug within the device is estimated to be 120 nL, while the minimum volume to be extracted out of the device would be between 0.5 and 1μL, largely determined by the minimum volume of standard pipettes, resulting in dilution. Therefore, in the design of this device, *in situ* concentration factor is less important than the overall flow throughput. If one can concentrate reliably from a 100mL volume of original sample, then the eventual concentration factor would be 10^5 or more (100mL / 1μL), regardless of *in situ* concentration factor observed by the microscope.

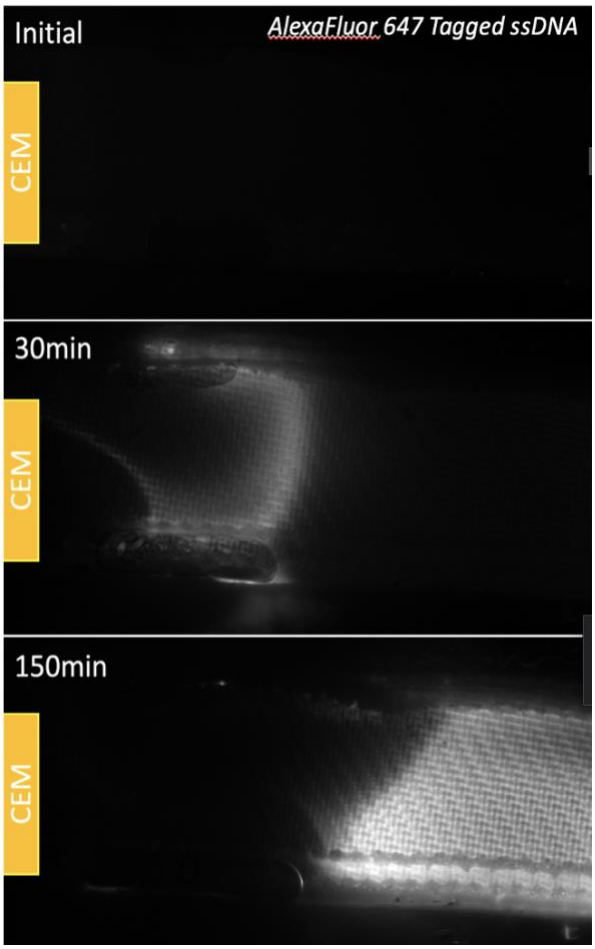

Figure 4-3 A sequence of images showing the formation and expansion of a concentration plug directly upstream of the depleting CEM. In the final image the concentration plug has expanded upstream and outside of microscope field of view.

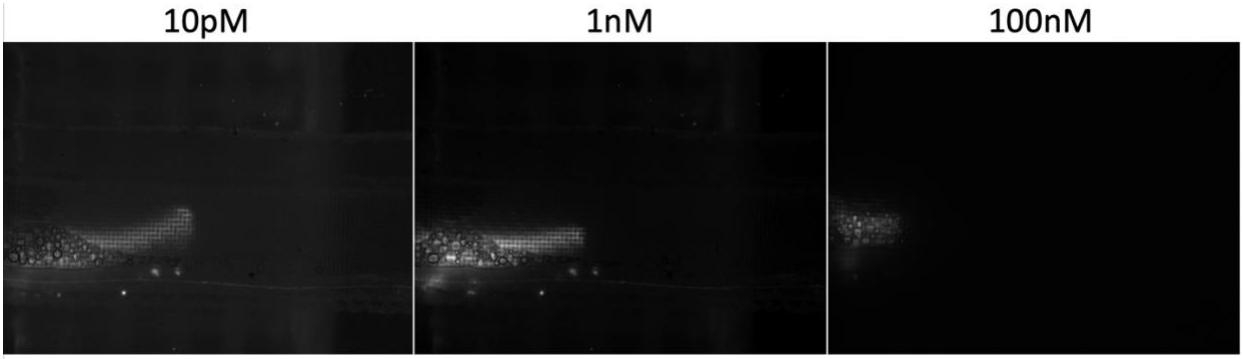

Figure 4-4 Images of the concentration plug formed after 30 minutes for three concentrations of ssDNA. The exposure time in the 10 pM and 1 nM images was 100 ms, while exposure time was 1 ms for the 100 nM image to avoid saturating the pixels.

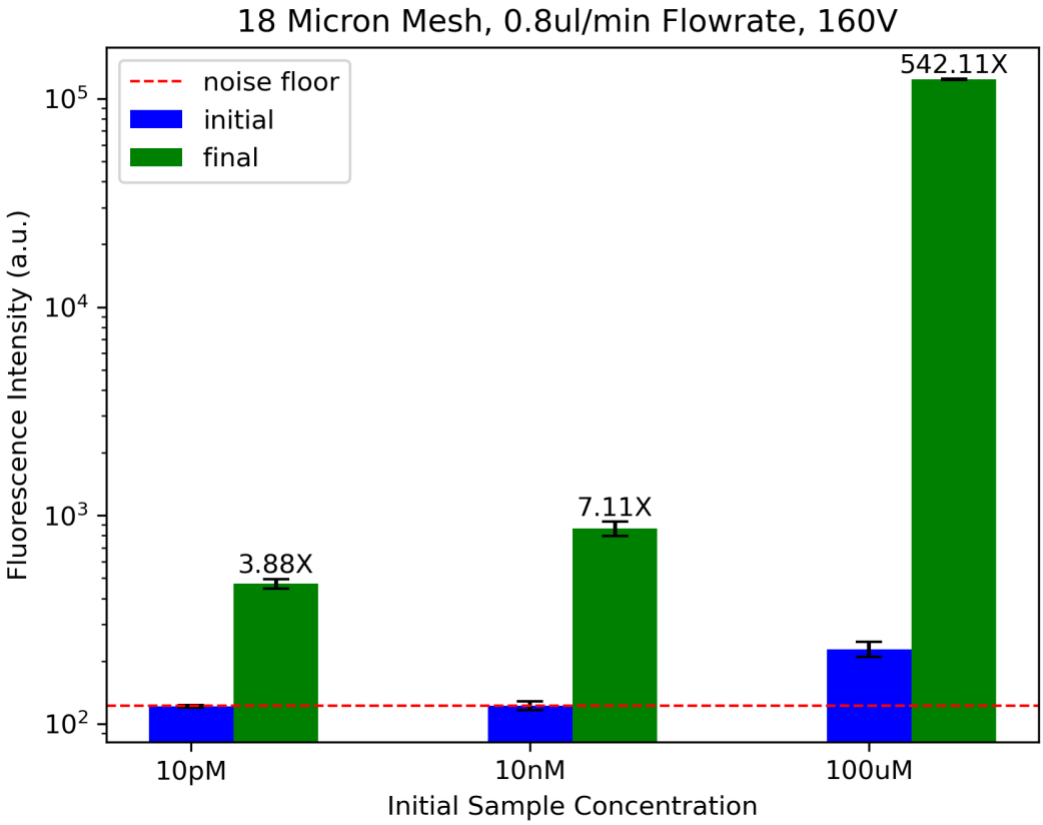

Figure 4-5 Plot showing the increase in fluorescence intensity after 30 minutes for a flowrate of 0.8 μL/min and 160V applied bias. Standard deviations were calculated using the peak values from the initial and final 3 minutes of a run respectively.

4.3 Effect of changing mesh dimensions

The size of the micropores in the device can be easily changed by replacing the nylon mesh in the main channel of the device. For each device two layers of mesh were placed inside the channel cutout in the adhesive/PET stack. Multiple mesh layers were used because each mesh was approximately half the thickness of the adhesive/PET stack, and the channel needed to be completely filled to ensure stability. A flowrate of 0.2 microliters per minute was selected to be the lowest flowrate tested so that a stable depletion region would be formed even for the large 35-micron pore size. A voltage bias of 200V was used for all flowrates so that a depletion region would be formed at some of the higher flowrates. The ssDNA concentration was 1nM and devices were operated for 1 hour at each flowrate. The best concentration factor achieved for each pore size can be seen in **Table 4-1.**

The concentration performance of the 35-micron pore size was poor compared to the other pore sizes and can be seen in **Figure 4-6a**. A significant concentration plug was only visible at the lowest flowrate, but the instability of the plug and leakage led to a concentration factor of only 7x. At all flowrates the depletion region was not stable and thus there was significant leakage. Evidence of this leakage can be seen in the current measurements shown in **Figure 4-7a.** At the lowest flowrate of 0.2 microliters per minute the current drops from its peak value and then spikes intermittently. These sudden increases in current occur when vortices generated by non-linear electroosmotic flow are not well

contained by the pores. The depletion region becomes diffuse and expands upstream and eventually the vortices lead to significant leakage that disrupts the depletion region, leading to device failure. At all other flowrates there was no significant decrease in current after reaching the peak voltage indicative of ICP phenomena and therefore there was only partial ion depletion in the channel.

The concentrating performance of the 18-micron pore mesh was significantly better, as seen in **Figure 4-6b**. A concentration factor of 51x was achieved for the flowrate of 0.9 microliters per minute, and concentration plug formation was observed for all flowrates except 7.2 microliters per minute. The smaller pore size of this mesh led to better confinement and stability of the depletion region, evidenced by the current plot **Figure 4-7b.** At the lowest flowrate the current reaches a peak and then decreases indicating ICP phenomena has occurred, and the current remains lower for the duration of the experiment indicating the depletion region is stable. However, at the higher flowrates there is no significant drop in current and more fluctuation in the current indicating the channel is partially depleted of ions and is not completely stable.

The 7-micron pore mesh performed the best overall by achieving higher concentration factors at higher flowrates than the other meshes, as seen in **Figure 4-6c**. At a flowrate of 1.8 microliters per minute a concentration factor of 227x was achieved, and a concentration plug was observed for all flowrates. The concentration factor achieved at 3.6 microliters per minute was 159x, which is significant because it is only 36% lower than the concentration factor achieved at half the flowrate. This means that the increase in leakage

was not exactly proportional to the increase in flowrate. In **Figure 4-7c** it can be seen that the 7-micron pore device at the lowest flowrate was also able to produce a decrease in current associated with the ion concentration polarization effect. At the other flowrates there was no significant drop in current, but the current was stable over time. This behavior indicates that the 7-micron pore device is better able to deplete the channel of ions and achieve a steady state than the larger pore devices. Thus, the smallest pore may still have leakage of analyte and not be able to fully generate a depletion region at high flowrates, but there is still net accumulation of analyte in areas of the device where the depletion region is well confined.

The superior performance of the smallest pore size agrees with the current understanding of EK concentrator design. Depletion regions are disrupted by the generation of large-scale vortices that cause leakage and device failure. Previous EK concentrators have been able to use channels that were hundreds of microns wide so long as the channels were only tens of microns deep to confine the vortices. Similarly, our device is able to use a millimeter wide channel that is hundreds of microns deep by confining the vortices within the micropores. It is worth noting that the concentration factor achieved by the 7-micron pore at the lowest flow rate was less than that of the 35-micron pore. This difference in performance is not because the smaller pore had greater leakage of analyte at the flowrate, but instead because the depletion region was able to expand and cause the concentration plug to diffuse upstream.

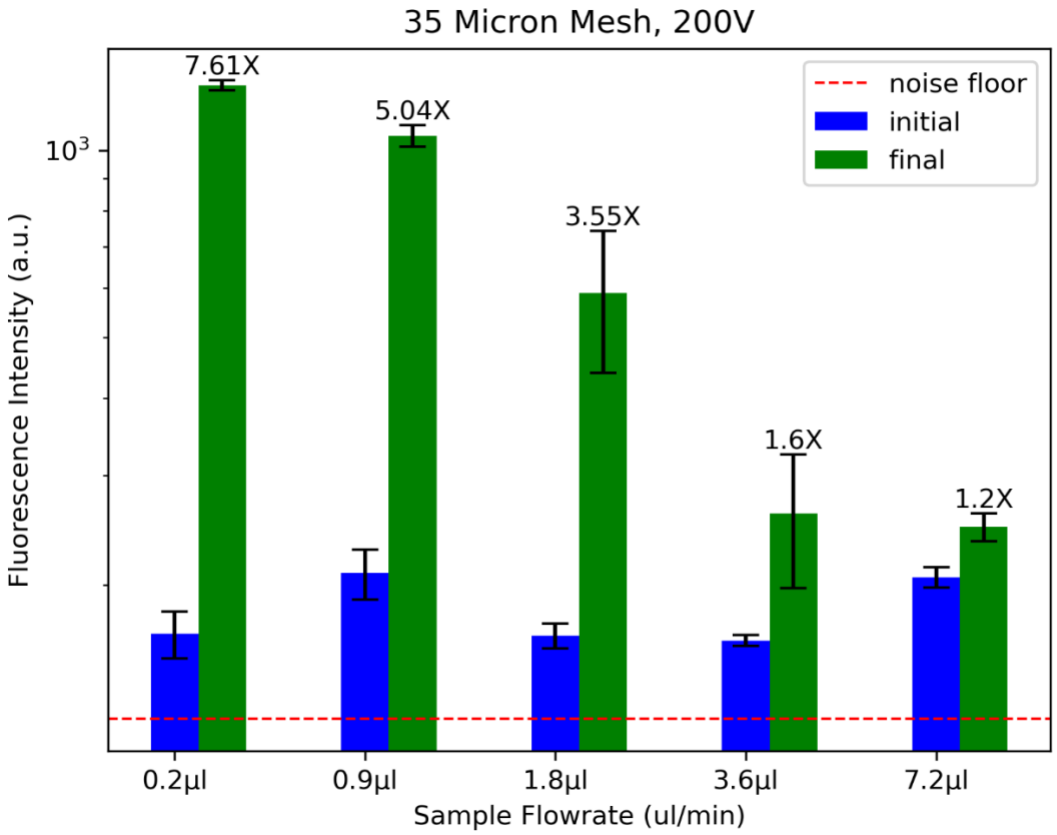

Figure 4-6a Plot showing the increase in fluorescence intensity of 1nM ssDNA after 1 hour for varying flowrates with applied bias of 200V and 35 µm mesh pore size. Standard deviations were calculated using the peak values from the initial and final 3 minutes of a run respectively.

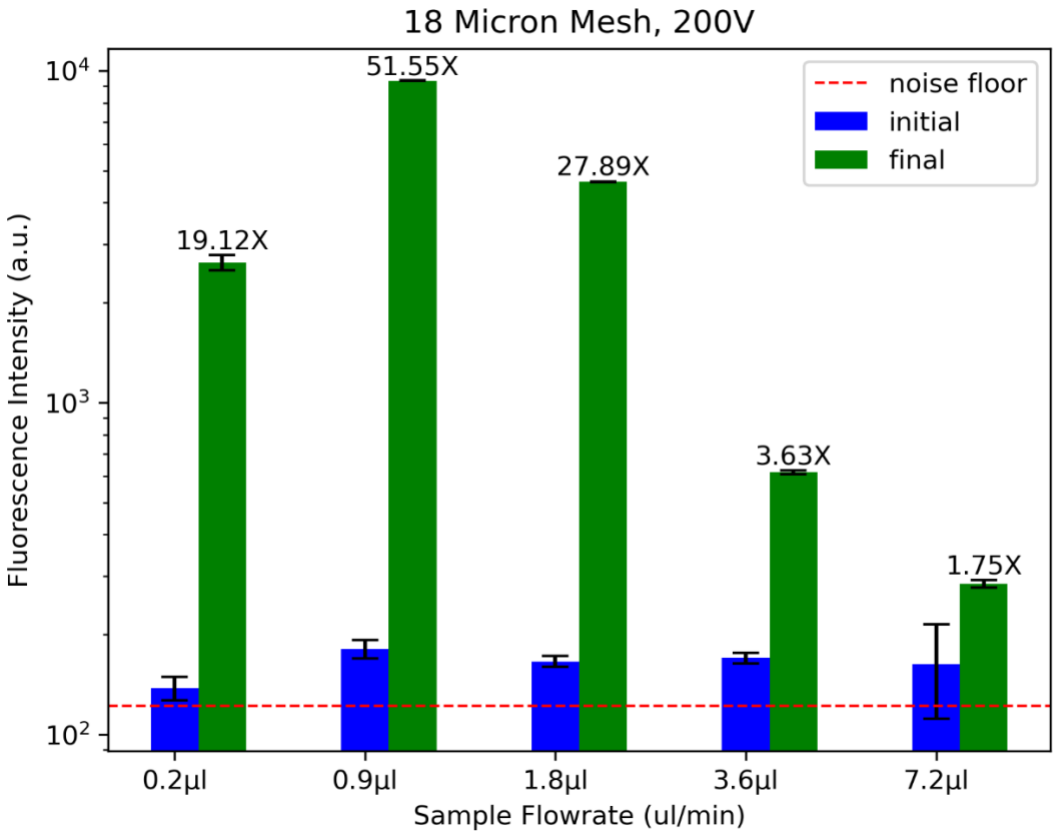

Figure 4-6b Plot showing the increase in fluorescence intensity of 1nM ssDNA after 1 hour for varying flowrates with applied bias of 200V and 18 µm mesh pore size. Standard deviations were calculated using the peak values from the initial and final 3 minutes of a run respectively.

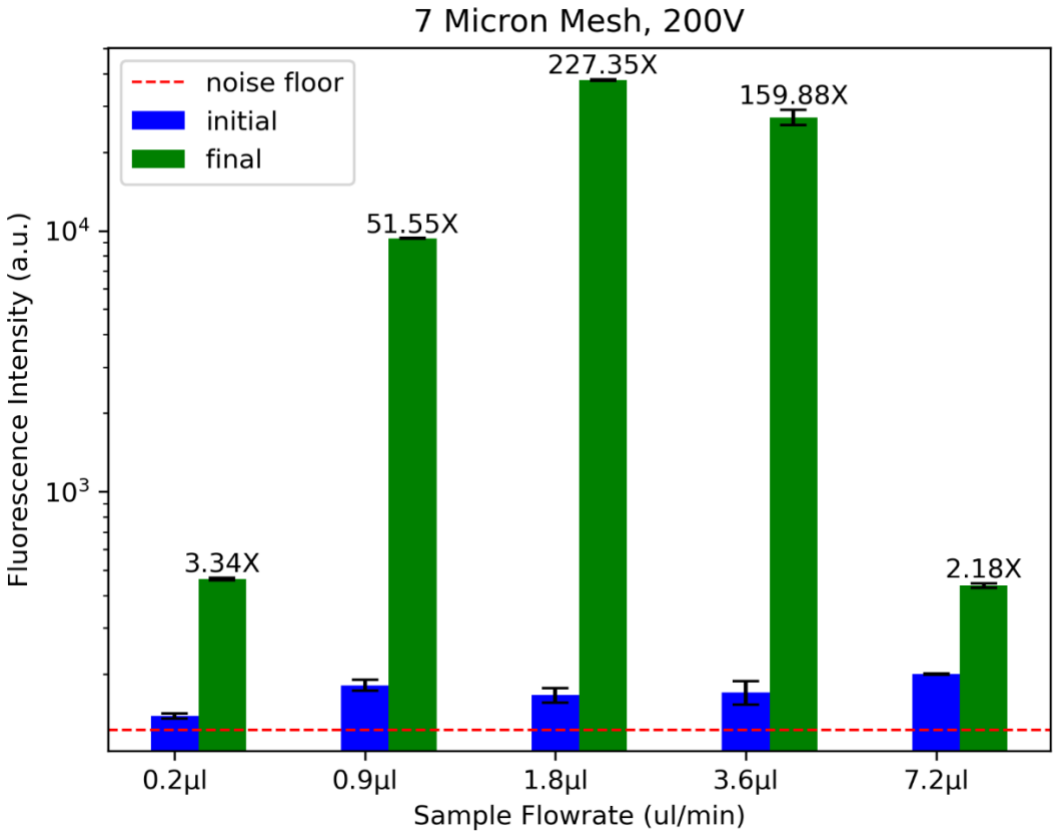

Figure 4-6c Plot showing the increase in fluorescence intensity of 1nM ssDNA after 1 hour for varying flowrates with applied bias of 200V and 7 μm mesh pore size. Standard deviations were calculated using the peak values from the initial and final 3 minutes of a run respectively.

Table 4-1

Pore Size	Peak CF
35μm	7x
18μm	51x
7μm	227x

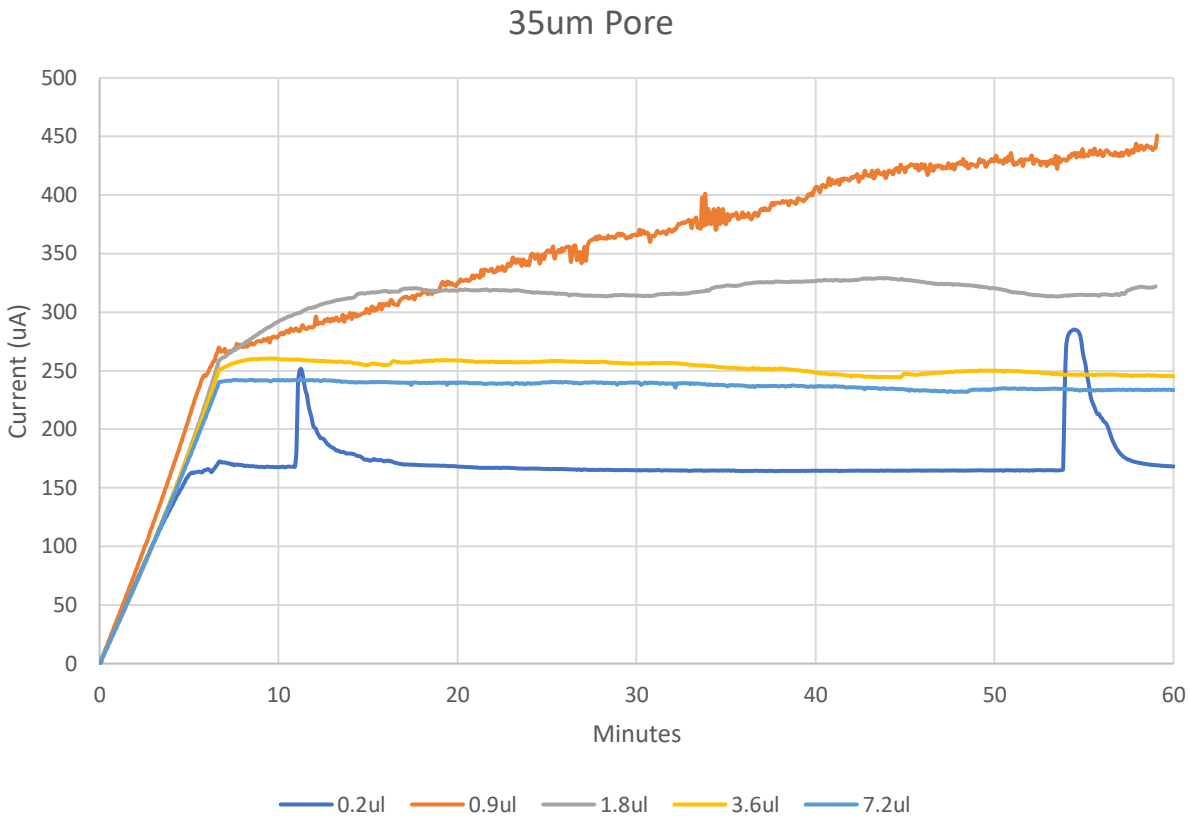

Figure 4-7a Plot of the current over 1 hour for varying flowrates with applied bias of 200V and 35 μm mesh pore size.

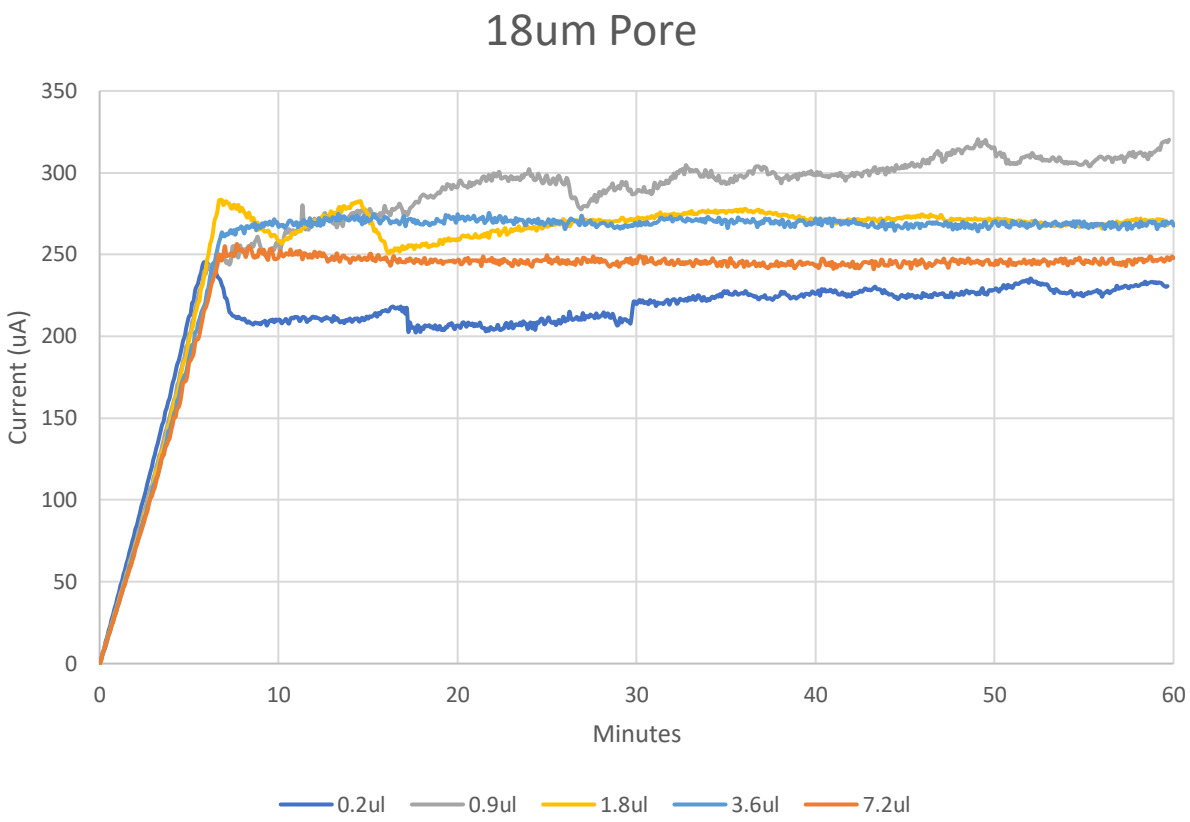

Figure 4-7b Plot of the current over 1 hour for varying flowrates with applied bias of 200V and 18μm mesh pore size.

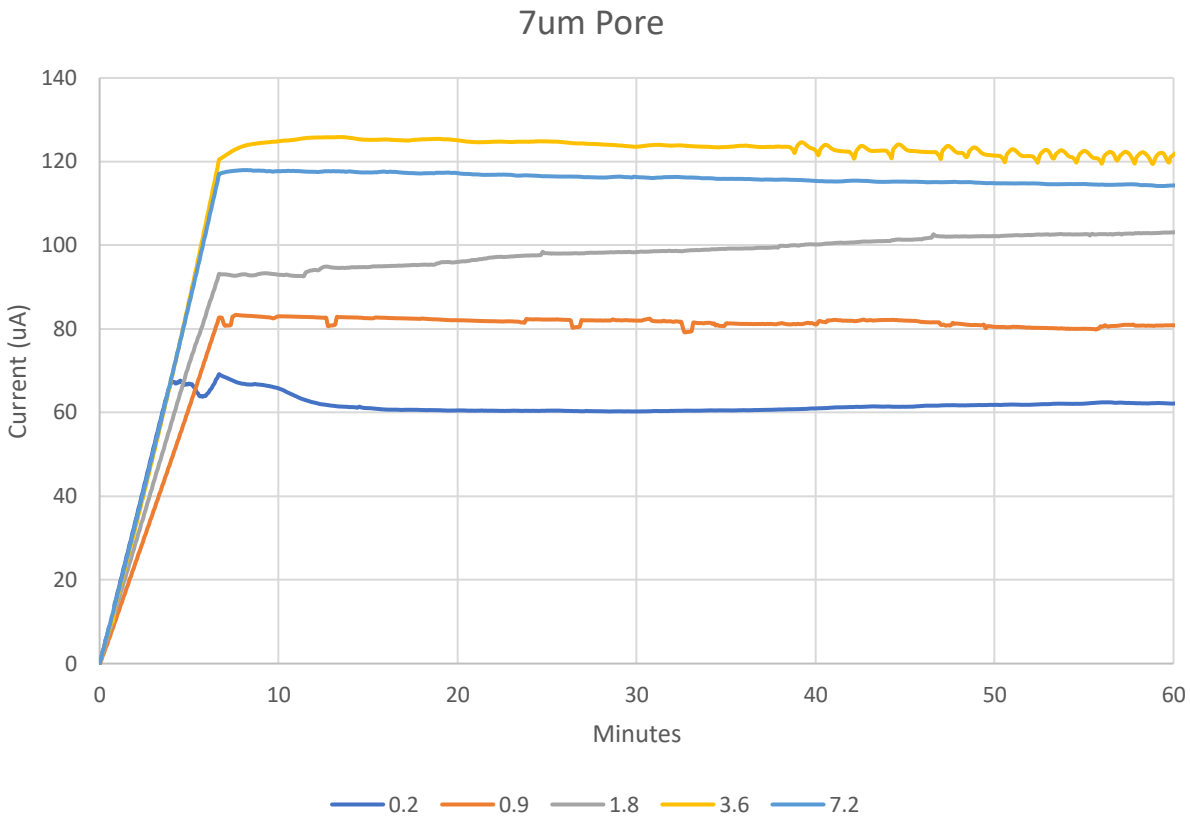

Figure 4-7c Plot of the current over 1 hour for varying flowrates with applied bias of 200V and 7 μm mesh pore size.

4.4 Effect of voltage bias on concentration performance

Devices with 7 micron and 18 micron pore sizes were operated for 30 minutes at varying voltages to characterize the effect of voltage bias on concentration and how it relates to the pore size. A low flow rate of 0.2 microliters per minute was selected to improve the likelihood of depletion region formation even at lower voltages. The fluorescently tagged DNA was used at a concentration of 10 pM so that the camera exposure time (100ms) would not have to be adjusted during the run.

The 18-micron pore device performed best at a bias of 160 V, as shown in **Figure 4-8a.** For the 7-micron pore device biases of 120V and 160V produced similar levels of peak fluorescence intensity, as shown in **Figure 4-8b.** The peak fluorescence intensity achieved at 200V in both devices was lower than other voltages because the depletion region began to expand and cause the plug to diffuse upstream. **Figure 4-9a** shows that the 18 micron pore is able to keep the current stable over time but there is not significant drop in current associated with the sudden formation of a depletion region. In **Figure 4-9b** the 7-micron pore device is able to produce a drop in current associated with the generation of a depletion region at every voltage tested except 40 V. Additionally, the time between reaching peak voltage and observing a drop in current decreases as the peak voltage increases, meaning higher voltage biases are able to deplete the channel of ions faster.

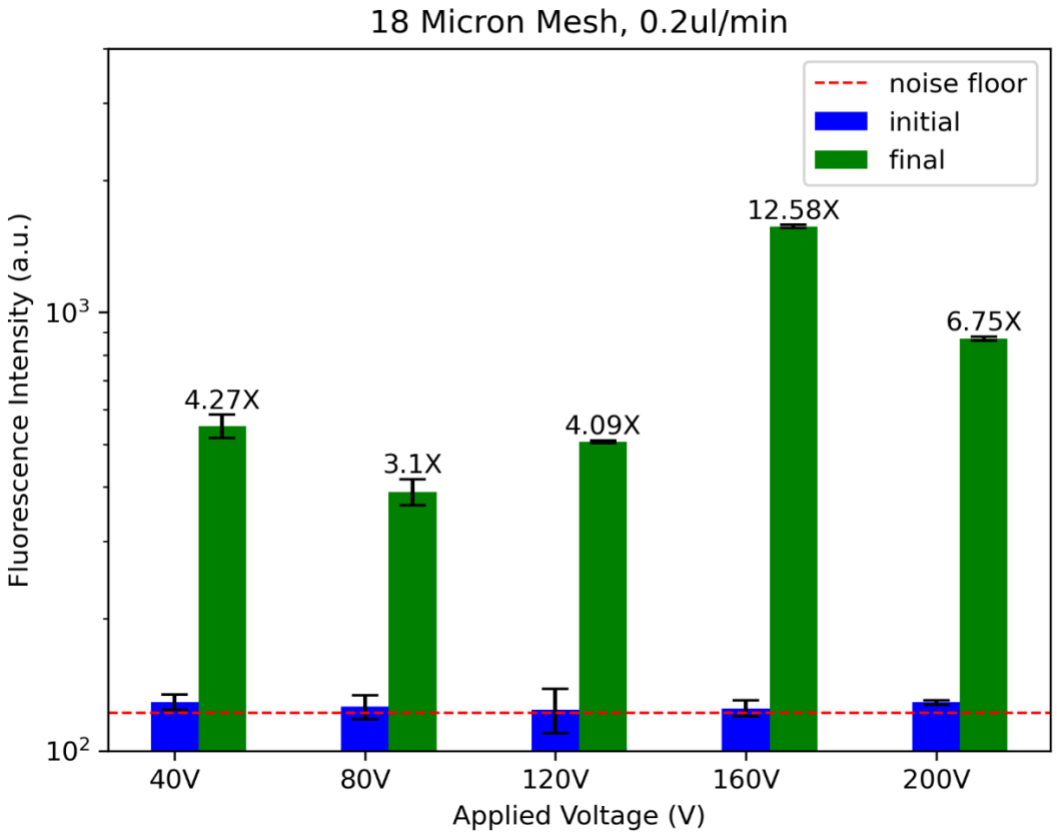

Figure 4-8a Plot showing the increase in fluorescence intensity of 10nM ssDNA after 30 minutes for varying voltage biases for 18 μm mesh pore size. Standard deviations were calculated using the peak values from the initial and final 3 minutes of a run respectively.

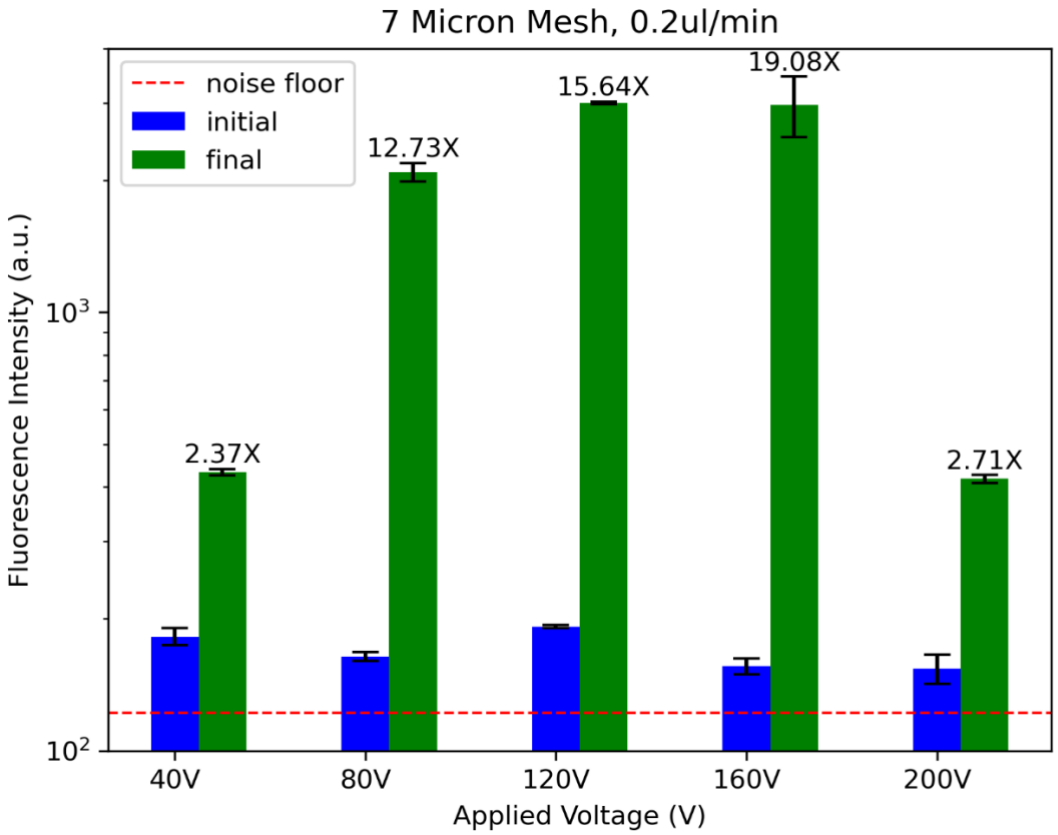

Figure 4-8b Plot showing the increase in fluorescence intensity of 10nM ssDNA after 30 minutes for varying voltage biases for 7 μm mesh pore size. Standard deviations were calculated using the peak values from the initial and final 3 minutes of a run respectively.

Figure 4-9a Plot of the current over 30 minutes for varying biases with flowrate 0.2 μL/min and 18 μm mesh pore size.

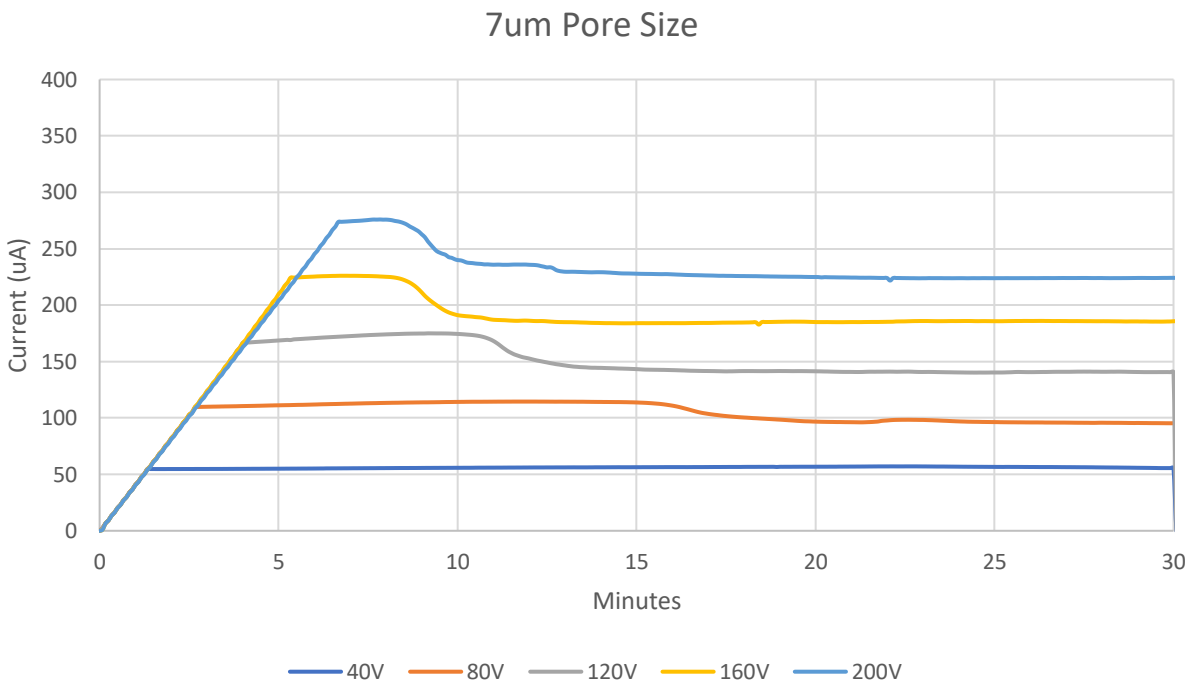

Figure 4-9b Plot of the current over 30 minutes for varying biases with flowrate 0.2 μL/min and 18 μm mesh pore size.

Chapter 5. Future Improvement

The materials and processes used to make the design discussed in the previous chapter can be easily adapted to other device configurations that may further improve manufacturability and concentration performance.

5.1 Laser etching for microchannel patterning

The use of PDMS molding on photolithographically patterned SU-8 has been the most prevalent technique used to define microfluidic channels[1–3]. As interest in larger scale microfluidic devices has increased there has been extensive research into using lasers to etch microfluidic channels into hard plastics such as PMMA[4–7]. Laser micromachining cannot match the lateral or vertical spatial resolution of SU-8 photolithography, but it is advantageous in several other respects. Deep channels—on the scale of millimeters—can be easily etched by simply increasing the laser power or decreasing the speed at which the laser passes over the substrate. In contrast, deep channels defined using SU-8 can require specialized spin-coating equipment and adjustments to the exposure and development process[8].

Characterization of laser etch (Universal Laser Systems VLS6.75 75 Watt CO_2) parameters were performed so that the etched channel depth could be closely matched to the thickness of a single mesh layer. A profilometer (Bruker DektakXT) was used to measure the depth of laser etched channels. For each set of laser cutting parameters an area of 1.5 mm by

1.5 mm was etched into the surface of a piece of PMMA. The profilometer tip was moved over 1.5 mm for each measurement, taking a path from the flat PMMA surface to the center of the etched area. To calculate the depth the z-position of the probe was averaged over 500 μm of the etched area and subtracted from the z-position average over 500 μm of the flat PMMA surface. This measurement process avoided incorporating the sloped edge of the etched area into the depth measurement by taking both averages in areas far from the edge. Laser parameters that produced channel depths greater than 1 mm were excluded because features of that scale risk damaging the profilometer stylus and are not relevant to the concentrator design.

The parameters involved in adjusting the depth of laser etching are the laser power, the speed that laser passes over the substrate, the 'quality parameter', and the pulses per inch (PPI). The quality parameter increases the density of lines in a raster image, so a higher quality image will cause the laser to make more passes over the etched area. The PPI controls the frequency with which the laser turns on while passing over the etched area.

The plot in **Figure 5-1** shows the expected trend of slower laser scan speeds producing deeper channels but it provides two other conclusions about the laser system. At the lower power settings—approximately zero to 40 percent—there is a nearly linear relationship between the channel depth and laser power. Additionally, the standard deviation of the channel depth increased as the power increased for all speeds tested. Based upon this information is was decided that the laser power should be kept in this low range and speed should be adjusted instead to make large changes in channel depth. In general, the quality

factor affects the slope of the linear relationship between channel depth and laser power, as seen in **Figure 5-2.** It is worth noting the highest quality factor of 7 produced a particularly rough surface with a standard deviation of ±142 μm when used at a power of 40%. The quality factor has less of an effect on channel depth than the laser speed. Therefore, it was decided to keep the quality factor constant at a value of 5 for device fabrication and to make adjustments to speed and power instead. The PPI parameter has little effect on the channel depth, as can be seen in **Figure 5-3.** Significant difference in the channel depth for differing PPI values was only seen at power of 50%, which is outside the ideal range of zero to 40% power that would be used for etching.

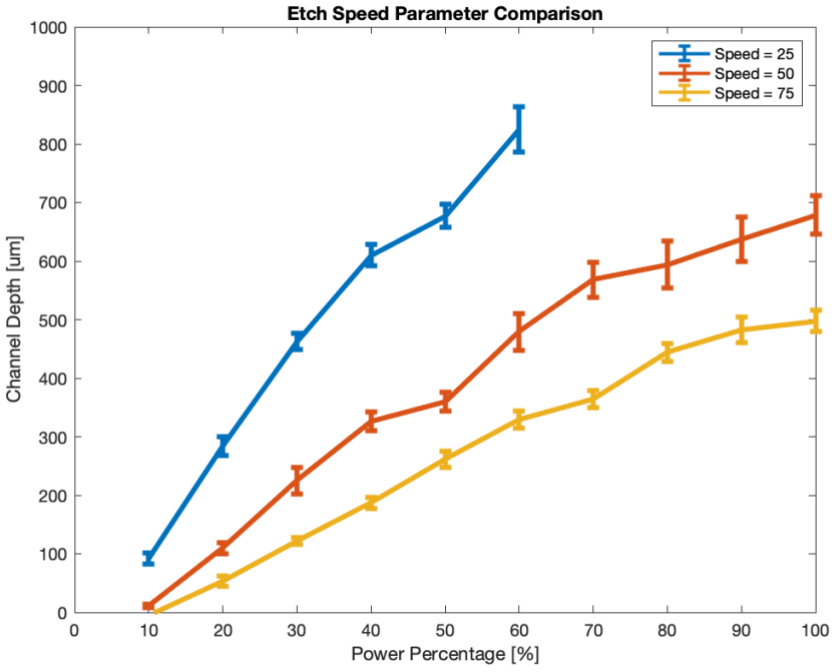

Figure 5-1 Plot of the relation between laser power settings and channel depth at three different speeds. PPI was set to 500 and the quality parameter was 5 for all etchings.

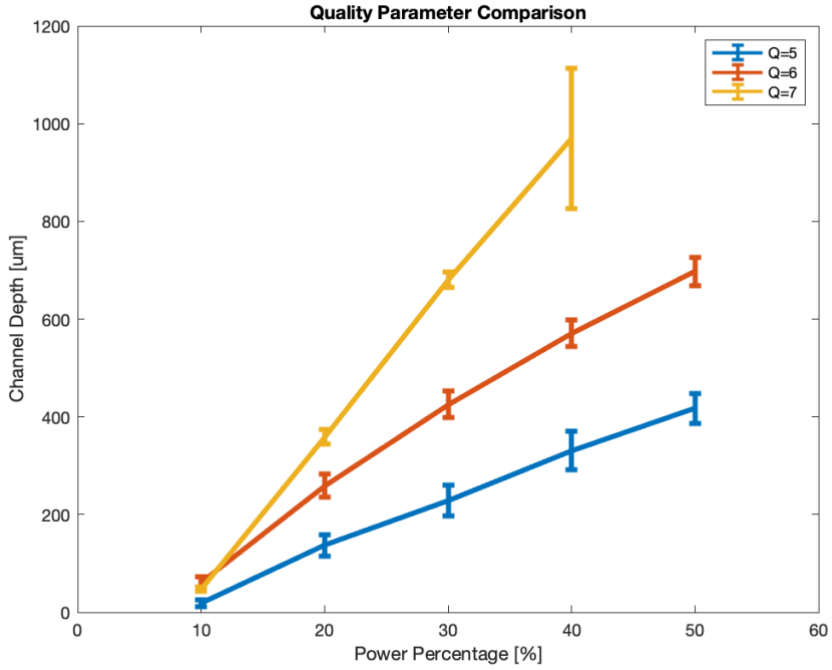

Figure 5-2 Plot of the relation between laser power settings and channel depth for three different quality parameters. The PPI was set to 1000 and the speed was 50% for all etchings.

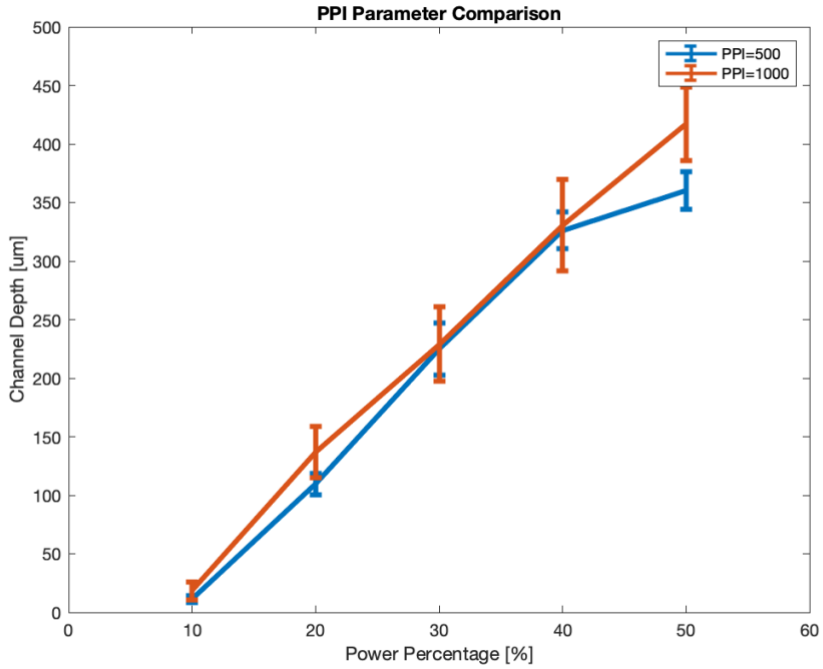

Figure 5-3 Plot of the relation between laser power settings and channel depth for two PPI settings. The speed was 50% and the quality parameter was 5 for all etchings.

5.2 Embedded Mesh Device

With the laser etching parameters characterized it was decided the manufacturing complexity of the EK concentrator can be further reduced by etching channels into the top and bottom PMMA layers of the device. A diagram of the improved device can be seen in **Figure 5-4.** The channels etched into the bottom layer were matched to the thickness of the 7-micron nylon so that a single layer of mesh could fill the channel near CEM. The mesh portion of the device was able to be reduced because at high enough flowrates the depletion region would not expand upstream and therefore the confinement of non-linear electroosmotic flow would only be needed near the depleting membrane. Channels with a depth of approximately 300 μm were etched into the top layer of PMMA to make connections between the inlet, outlet, and mesh IEM junction regions. Having the channels etched into the acrylic surfaces allowed for the elimination of one of the adhesive-PET stacks, further simplifying the device. The stability of the simplified device was not decreased as **Figure 5-5** shows the device accumulating a stable concentration plug over 4 hours at a flow rate of one microliter per minute. Characterization of the concentration factor after 30 minutes and the same flowrate can be seen in **Figure 5-6** with a value of 162x being achieved.

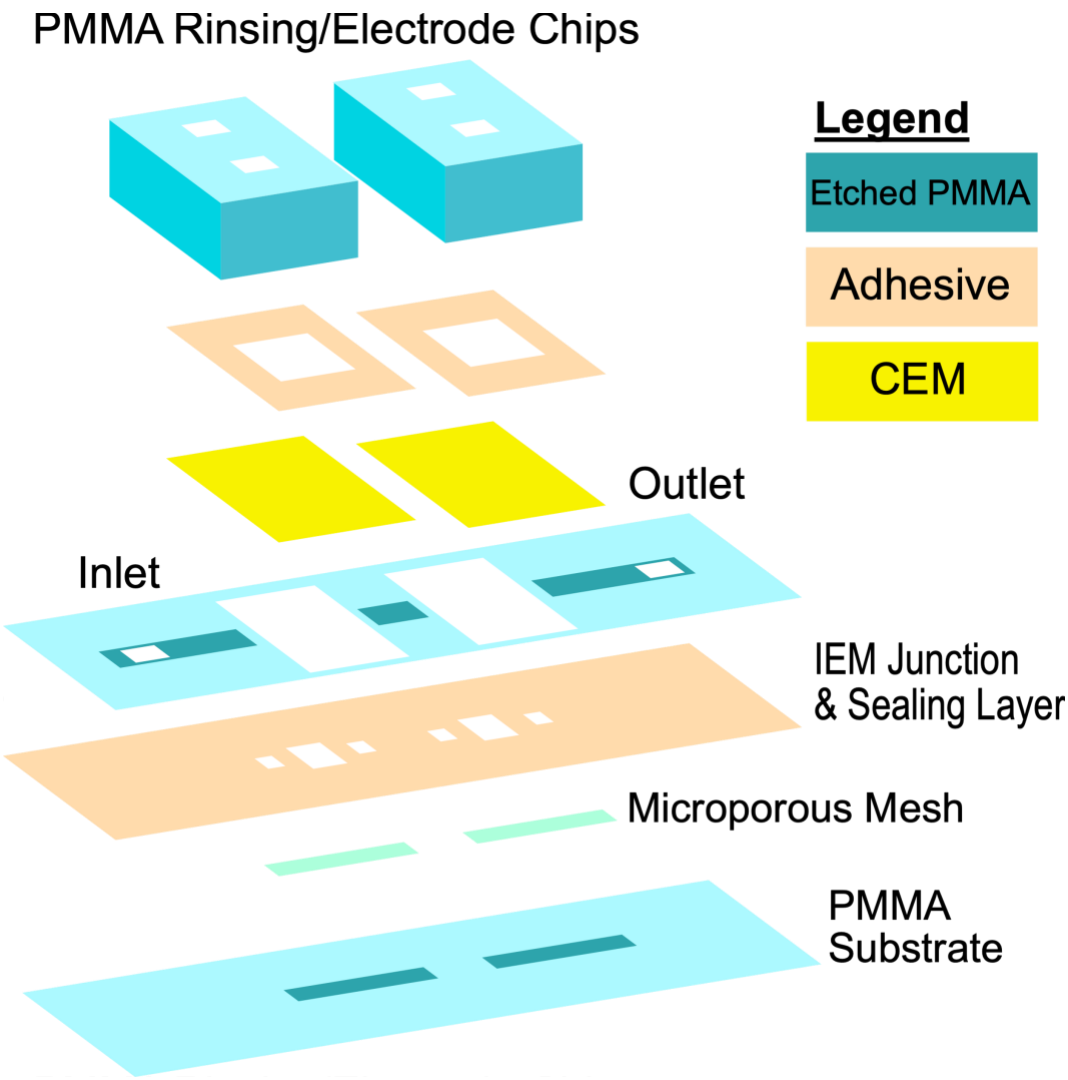

Figure 5-4 A diagram of the embedded mesh concentrator.

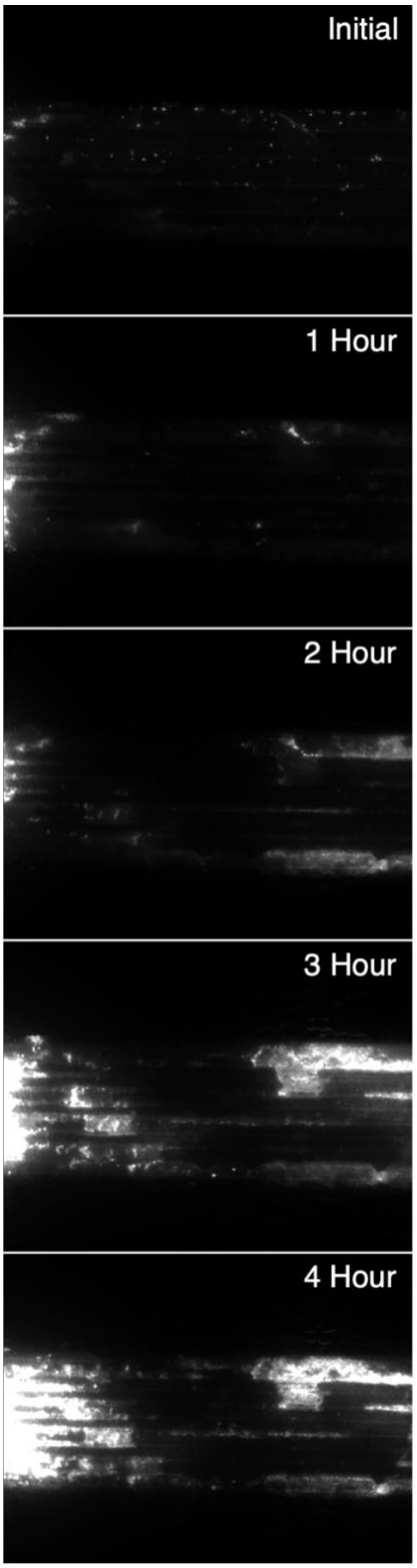

Figure 5-5 A sequence of images showing the formation and expansion of a concentration plug directly upstream of the depleting CEM over 4 hours.

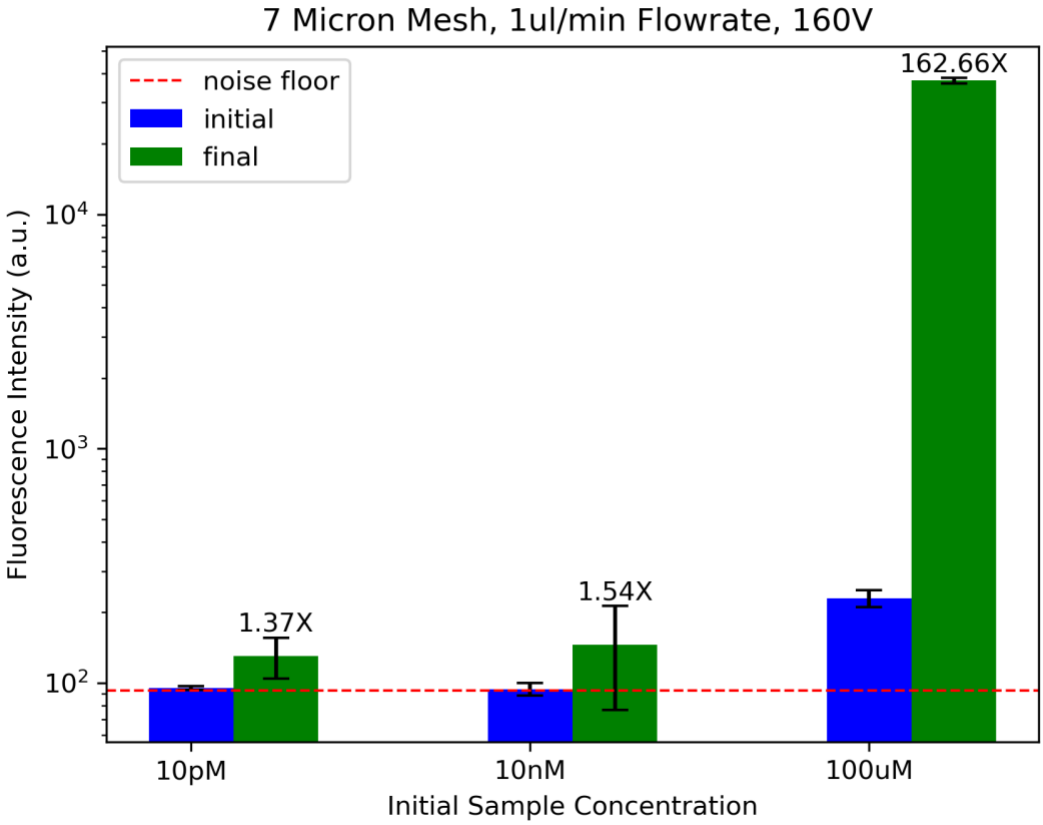

Figure 5-6 Plot showing the increase in fluorescence intensity after 30 minutes for a flowrate of 1 μL/min and 160V applied bias. Standard deviations were calculated using the peak values from the initial and final 3 minutes of a run respectively.

5.3 Heterogeneous AEM/CEM Device

Though nearly all EK concentrators utilize a single CEM there has been some work in the past to explore devices that use two different ion exchange membranes—creating a heterogeneous junction[9]. By using an anion exchange membrane (AEM) and CEM both ionic species can be removed or added to the channel, potentially increasing the stability of devices by generating more ion depletion in the channel. However, work with heterogenous

devices was difficult to expand upon because there is no commercially available liquid AEM resin, so ion selective hydrogels had to be fabricated that were compatible with the surface flow patterning method.

Fortunately, there are many commercially available solid AEM membranes that are used in fuel cells, desalination, and electrodialysis applications. Our fabrication method is generalizable to any solid membrane because the seals are mechanical and not chemical, therefore it would be easy to explore more heterogeneous designs. A schematic of a potential device can be seen in **Figure 5-7** in which anions are extracted upstream and cations downstream, creating a region highly depleted of ions between the two membranes. Similar to the dual CEM design this device can be operated by placing electrodes in the membrane rinsing channels—isolating them from the sample—and setting the AEM channel to a higher voltage than the CEM channel.

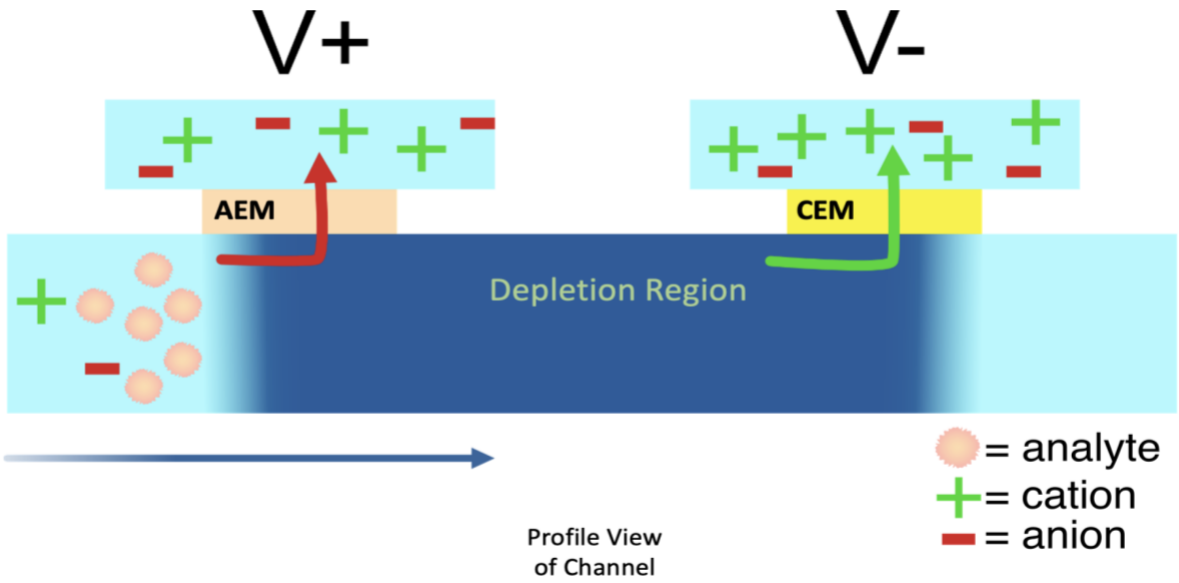

Figure 5-7 High level schematic of the AEM-CEM concentration device.

5.4 References

1. Xia, Y. & Whitesides, G. M. Soft lithography. *Angew. Chemie - Int. Ed.* **37**, 550–575 (1998).
2. Lee, J. B., Choi, K. H. & Yoo, K. Innovative SU-8 lithography techniques and their applications. *Micromachines* **6**, 1–18 (2015).
3. Raj M, K. & Chakraborty, S. PDMS microfluidics: A mini review. *J. Appl. Polym. Sci.* **137**, (2020).
4. Chen, X., Li, T. & Shen, J. CO2 Laser Ablation of Microchannel on PMMA Substrate for Effective Fabrication of Microfluidic Chips. *Int. Polym. Process.* **31**, 233–238 (2016).
5. Bilican, I. & Tahsin Guler, M. Assessment of PMMA and polystyrene based microfluidic chips fabricated using CO2 laser machining. *Appl. Surf. Sci.* **534**, 147642 (2020).
6. Huang, Y., Liu, S., Yang, W. & Yu, C. Surface roughness analysis and improvement of PMMA-based microfluidic chip chambers by CO 2 laser cutting. *Appl. Surf. Sci.* **256**, 1675–1678 (2010).
7. Chen, X., Shen, J. & Zhou, M. Rapid fabrication of a four-layer PMMA-based microfluidic chip using CO2-laser micromachining and thermal bonding. *J. Micromechanics Microengineering* **26**, 1–7 (2016).
8. Lin, C. H., Lee, G. Bin, Chang, B. W. & Chang, G. L. A new fabrication process for ultra-thick microfluidic microstructures utilizing SU-8 photoresist. *J. Micromechanics Microengineering* **12**, 590–597 (2002).
9. Kim, P., Kim, S. J., Han, J. & Suh, K. Y. Stabilization of ion concentration polarization using a heterogeneous nanoporous junction. *Nano Lett.* **10**, 16–23 (2010).

Chapter 6. Conclusion

We have demonstrated a new electrokinetic concentrator design that has key advantages over previous devices in terms of manufacturability, sample throughput, and reliability. Translating electrokinetic concentrator technology to be constructed from off-the-shelf low-cost materials using a high-throughput manufacturing processes could help bring this technology closer to being deployed for several applications in which proof-of-concept devices have already proven to be useful. Our device also acts as an example for future designs that eschew traditional microchannels in favor of large channels filled with microporous structures. The general materials and processes used to build the devices explored in this work could easily be adapted to other configurations that may improve sample throughput, power consumption, or interface with specific detection technologies.